inorganics

MDPI

Article

Photovoltaic-Relevant Optical and Dielectric Behavior of the Azo-Oxime Ligand and Its VO^{2+}-, Cu^{2+}-, and Fe^{3+}-Based Complexes Films

Kamal A. Aly *, Tahani M. Shatir and Mohamad M. Ebrahium

Applied College at Khulais, University of Jeddah, Jeddah 21589, Saudi Arabia; tshater@uj.edu.sa (T.M.S.)
* Correspondence: kaali5@uj.edu.sa

Abstract

Cu^{2+}, VO_2^{2+}, and Fe^{3+} mononuclear complexes of the oxime-based ligand, 2-hydroxy-5-(*p*-tolyldiazenyl)benzaldehyde oxime (H_2L, **1**), have been synthesized and structurally characterized by analytical, thermal, and spectral tools. They have been characterized by microanalyses (C, H, and N), ^1H and ^{13}C-NMR, FT-IR, UV-Vis, and/or ESR spectral measurements. The various analytics data indicate that the oxime-based ligand behaved as a neutral bidentate chelator binding Cu^{2+}, VO^{2+}, and Fe^{3+} cations via the nitrogen atom of the protonated oximatic group and protonated phenolic hydroxyl oxygen atom, adopting a distorted octahedral geometry. Furthermore, computational studies utilizing DFT/B3LYP/6-311(pd) include assessment of dipole moment, global reactivity descriptors, optimized geometry, LUMO-HOMO energy gaps, and molecular electrostatic potential image (MEP), which were estimated to support the geometrical structure of Cu^{2+}, VO^{2+}, and Fe^{3+} complexes. Furthermore, the optical parameters, viz. the refractive index (*n*) and extinction coefficient of azo-oxime ligand and its complexes, have been precisely estimated within a 300–1100 nm wavelength. The values of optical gap (E_{gap}) for the azo-oxime ligand and its complex films diminished from 2.96 eV for H_2L to 1.83 eV for the Fe^{3+} film; however; the n values follow an opposite behavior. The obtained n and E_g values are comparable to those reported for various semiconducting materials, suggesting the potential suitability of the investigated films for future semiconductor and optoelectronic applications. Although practical device performance remains to be evaluated, these low-cost and easily prepared materials could serve as promising candidates in these fields. Furthermore, the dielectric and nonlinear optical parameters have been thoroughly evaluated and comprehensively discussed.

Keywords: azo-oxime; DFT; metal complexes; optics; non-linear optics; solar cells

Academic Editors: Sake Wang, Minglei Sun and Tuan-Hung Nguyen

Received: 9 August 2026
Revised: 8 September 2026
Accepted: 13 September 2026
Published: 18 September 2026

1. Introduction

The growing global demand for alternative and renewable energy sources in the modern era of green energy has driven rapid advancements in the creation of economical and effective technologies for energy conversion and storage [1]. Among these technologies, solar cells are of particular importance as they convert solar radiation into electrical energy. Although maximizing power conversion efficiency remains a key goal, overcoming challenges related to energy storage and transport is equally critical. In this context, electrochemical energy storage systems—such as supercapacitors and batteries—have demonstrated highly effectiveness in storing electricity created from alternative and renewable energy sources. Consequently, extensive study has been devoted to the development of

storage devices characterized by high energy and power densities, rapid charge–discharge rates, and long-term stability under optimal operational conditions. To further enhance the efficiency of energy conversion and storage systems, many approaches have been projected for the creation of photosensitive materials with superior properties [2]. Recently, coordination compounds and Metal–Organic Frameworks have attracted considerable attention as a new class of functional substances exhibiting distinct structural, electronic, and optical characteristics, making them suitable for advanced energy-related applications [3–6]. Coordination chemistry has experienced remarkable growth over the past decades, producing a broad diversity of metal-chelated complexes that find applications in electronic [7], optical [8], analytical [9], sensing [10,11], catalytic [12], biological [13], clinical [14], and industrial [15] fields. Current research efforts are increasingly directed toward the design of new organic chelating agents that act as molecular scaffolds for the creation of metallic complexes with desirable physicochemical properties. These metallic complexes have demonstrated potential in supercapacitors, solar cells, sensors, and electrochemical energy storage systems [16,17]. Among these ligands, oxime-based ligands occupy a distinctive position in coordination chemistry owing to the versatile donor character of their >C=N–OH functional group, which enables coordination to transition-metallic ions via the imine nitrogen, the oximato oxygen, or both, depending on the degree of deprotonation and the nature of the metal center [18,19]. This dual donor capability, combined with the ease of introducing additional functional groups (phenolic, azo, or aromatic substituents) onto the oxime backbone, has made oxime and azo-oxime ligands a widely exploited scaffold for constructing stable mononuclear and polynuclear metal complexes. Their strong chelating ability, structural tunability, and straightforward synthetic accessibility have established oxime-derived complexes as important targets across sensing, catalytic, biological, and materials-chemistry applications [20,21]. While the ultimate electrochemical and optoelectronic performance of devices depends heavily on the practical optimization of electrode and active layer materials, exploring the fundamental optical and electronic properties of novel organometallic complexes is a crucial preliminary step [22]. In this context, a series of VO^{2+}, Cu^{2+}, and Fe^{3+} complexes derived from the azo-oxime ligand, 2-hydroxy-5-(*p*-tolyldiazenyl)benzaldehyde oxime (H_2L, **1**) were synthesized via a simple and efficient method. These complexes were investigated to assess their fundamental optical parameters and evaluate their preliminary suitability as potential candidates for prospective optical switching, signal processing, and modulator applications. Their physicochemical properties were comprehensively characterized using analytical and spectral tools, including FT-IR, UV–Vis, NMR, and ESR Furthermore, Density Functional Theory (DFT) calculations at the B3LYP level employing the 6-311G(d,p) basis set were conducted to investigate the chemical reactivity, charge distribution, and molecular electrostatic potential (MEP) parameters. In addition, the energy loss functions and optical constants of the prepared thin films were thoroughly examined to elucidate their electronic and optical behaviors, thereby providing a foundational baseline for their potential future integration into semiconductor and photovoltaic devices.

2. Results and Discussion

2.1. Exploration of the Structure of Azo-Oxime and Its Cu^{2+}, VO^{2+}, and Fe^{3+} Complexes

The physical, analytical, and spectral properties of the synthetics were collected in the experimental part. The ligand 2-hydroxy-5-(*p*-tolyldiazenyl)benzaldehyde oxime ligand (H_2L, **1**) was reacted with the salts of Cu^{2+}, VO^{2+}, and Fe^{3+} forming mononuclear complexes with general formulae $[M(H_2L)XYZ_2].nH_2O$ (M = Cu^{2+}, X = Y = OAc^- or NO_3^-, Z = H_2O, X = SO_4^{2-},Y = H_2O, Z = 0; M = VO^{2+}, X = SO_4^{2-}, Z = H_2O, Y = 0; and M = Fe^{3+}, X = Z = Cl, Y = H_2O) as displayed in Figure 1a–c. The structures of the synthesized compounds were

elucidated using analytical, theoretical, thermal, and various spectroscopic techniques, including ^{1}H NMR, ^{13}C NMR, UV–Vis, and FT-IR. The results obtained from experimental measurements and theoretical calculations are presented in the experimental section and Tables 1–5, S1 and S2. The synthesized compounds are non-hygroscopic solids and remain stable at ambient temperature. The solubility test showed that the ligand is soluble in polar organic solvents, while the complexes are slightly soluble in well-known organic solvents but soluble in DMF and DMSO. Crystals suitable for X-ray diffraction studies were, unfortunately, not obtained. Elemental analysis confirmed the proposed molecular formulas and indicated that all chelated compounds (**2**–**6**) were formed in a 1:1 ligand-to-metal (L:M) molar ratio (Figure 1a–c).

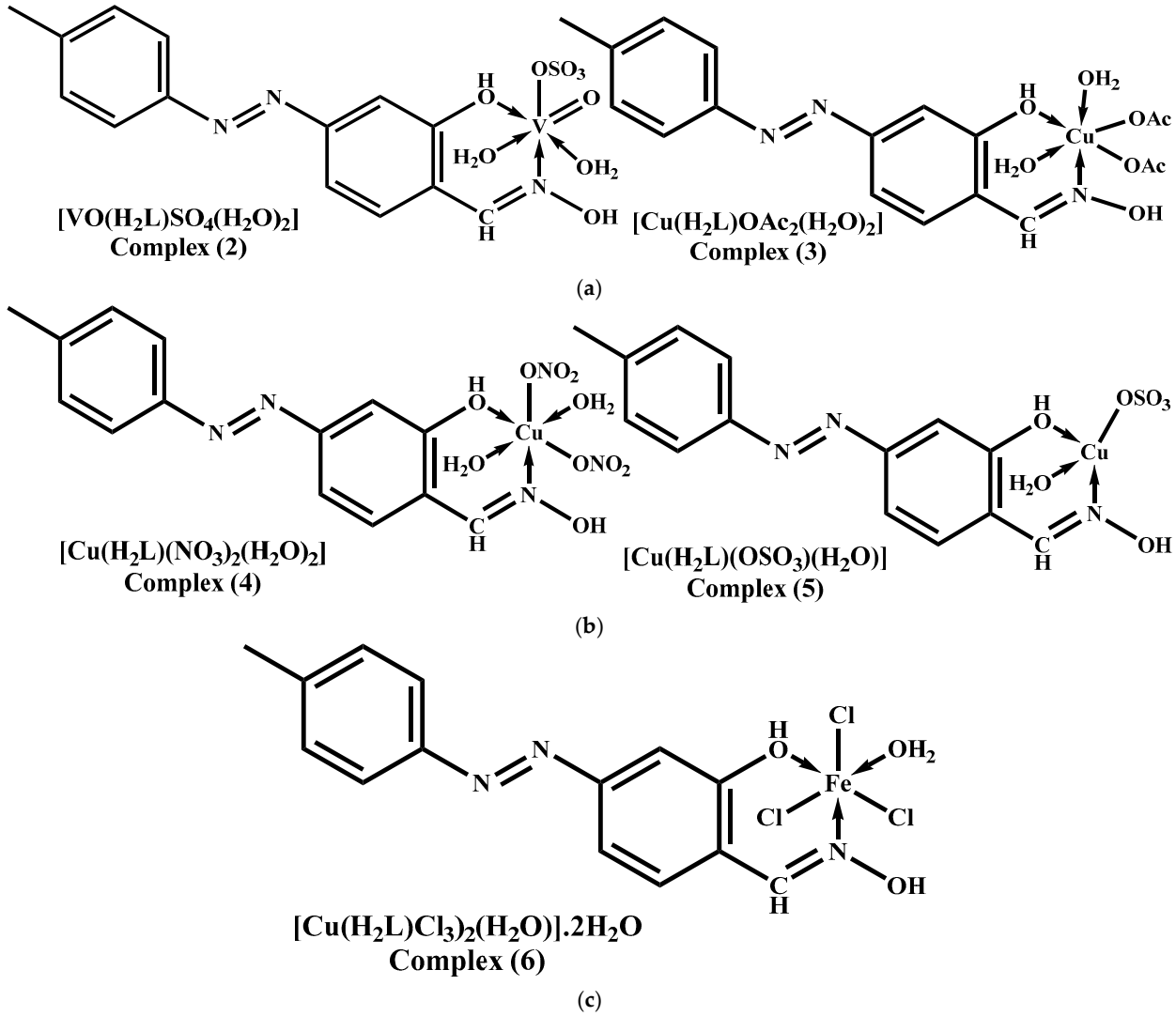

Figure 1. (**a**) Structure representation of VO^{2+} and Cu^{2+}, complexes (**2**,**3**). (**b**) Structure representation of Cu^{2+} complexes (**4**,**5**). (**c**) Structure representation of Fe^{3+} complexes (**6**).

Molar Conductivity

The values of molar conductance of complexes' solution (10^{-3} M, DMSO/25 °C) demonstrate a non-electrolytic nature, as evidenced by their relatively low molar conductance values in DMSO solution (Λ_M = 13.1–24.1 $\Omega^{-1}cm^2mol^{-1}$). This suggests a direct connection between the acetate, nitrate, sulphate, or chloride ions and the metallic cations [23]. The significantly high value may be due to the partial solvolysis by the solvent molecule [23].

2.2. Spectroscopic Studies

2.2.1. FT-IR Spectra

The main FT-IR data of synthetics is recorded in experimental parts and shown in Figures S1–S4. The chelation centers', (OH and C=N-OH), vibrational stretching is accountable for the significant bands seen in the synthetics' spectrum. In the free azo-oxime (H_2L, **1**) spectrum, the band observed at 1280, and 3400 cm^{-1} could be attributed to the bending δ(OH) and stretching ν(OH) bands successively [24,25]. Meanwhile, the stretching vibration at 1620 and 1010 cm^{-1} could be attributed to imine ν(C=N) and oximato ν(N-O) groups successively [24–26]. Additionally, the vibrational stretching of aliphatic and aromatic hydrogens was shown as weak bands at 3060, 3023, 2920, and 2849 cm^{-1} [25]. The chelation behavior of azo-oxime (H_2L, **1**) with VO^{2+}, Cu^{2+}, and Fe^{3+} has been recognizable by contrasting the IR spectra of VO^{2+}, Cu^{2+}, and Fe^{3+} complexes with that of unchelated azo-oxime. The chelation mode of azo-oxime with VO^{2+}, Cu^{2+}, and Fe^{3+} cations can be determined by comparing the complexes FT-IR with that of the free azo-oxime. It explained that the azo oxime (H_2L, **1**) interacts with VO^{2+}, Cu^{2+}, and Fe^{3+} cations as a neutral ON bidentate chelator chelated via the oxygen atom of the phenolic hydroxyl oxygen and the oximatic nitrogen of the imine groups. This mode was confirmed by several remarks as follows.

(i) The stretching frequency of the imine group was negatively shifted by 25–47 cm^{-1}.
(ii) The stretching band of the oximatic hydroxyl group appears at nearly the same position and the stretching band of the oximatic linkage (N-OH) shifts positively by 40–100 cm^{-1}, indicating that the oximatic moiety participates in chelation in its protonated form through the nitrogen atom rather than the oxygen atom [27].
(iii) The stretching band of the phenolic hydroxyl group appears at nearly the same position. This conclusion is underscored by the positive shift in the position of the bending υ(C-OH) band by 15–38 cm^{-1} [28].
(iv) The new stretching frequencies in the ranges 510–580 and 473–483 cm^{-1} may be inductively related to the ν(Mš←O) and ν(M←N) successively [29].

According to the literature, aromatic C–H stretching vibrations generally appear around 3000 cm^{-1}, whereas aliphatic C–H vibrations occur in the 2990–2800 cm^{-1} region. In the present study, the symmetric aromatic C–H stretching bands are observed in the 3000–3060 cm^{-1} range, whereas the asymmetric and symmetric aliphatic C–H stretching bands appear in the 2916–2980 cm^{-1} and 2850–2873 cm^{-1} regions, respectively [30]. Infrared spectra of the vanadyl and complex disclosed a medium band at 963 cm^{-1} attributed to ν(V=O) [31].

Anions Investigation

In the free acetate, there are two stretching vibrations at ca 1560 and 1416 cm^{-1}, attributed to $\nu_s(CO_2^{2-})$ and νas(CO_2^{2-}) respectively. The aetate anions can be bound to a metallic cation in one of three modes: unidentate, bidentate, or bridging. In an unidentate manner, ν_s(C=O) is larger than $\nu_s(CO_2^{2-})$ while ν(C-O) is lesser than $\nu_{as}(CO_2^{2-})$. In turn, the separation between the two $\nu_{as}(CO_2^{2-})$ and $\nu_s(CO_2^{-})$ is significantly greater in unidentate than in free acetate anion, but bidentate has less separation than in the free ion; however, in the bridging bidentate the two $\nu_{as}(CO_2^{2-})$ and $\nu_s(CO_2^{2-})$ are close to the free anion [31,32]. In the acetate complex (**3**), the symmetric and asymmetric stretching of the acetate anion is seen at 1540, and 1350 cm^{-1}. The difference (190 cm^{-1}) specifies that the acetate bonded to Cu^{2+} cation in a unidentate fashion [31,32]. The ands at ν_5(1409), ν_1(1345), and ν_2(920) in the IR spectrum of nitrato complex (**4**) signify that the nitrate anion was directly attached to the metallic ion. The difference (ν_5–ν_1) is 64 cm^{-1}, signifying that nitrate anion acts as a unidentate chelator. The sulfato complex (**5**) has two bands at 1190

and 1055 cm^{-1} in its infrared spectra, attributed to the mono-chelated sulfate group, as seen by their low conductivity value [31,33].

2.2.2. Nuclear Magnetic Resonance (NMR)

To identify the azo-oxime ligand's coordination mode with the metallic cations and to obtain valuable insights about its structure, the azo-oxime's NMR spectrum was measured in DMSO-d_6, and its chemical shifts are explained and summarized in the experimental parts based on the atomic labeling shown in Figure 2. The azo-oxime's ^1H NMR spectrum (Figure S5) unveiled two slightly broad singlets at 11.54 and 11.06 ppm, corresponding to the protons of the phenolic and oximatic hydroxyl groups, respectively; both signals disappeared upon the addition of D_2O. A downfield signal observed at 8.40 ppm was assigned to the imine proton. The overlapping CH signals appearing in the 8.11–7.16 ppm range were attributed to the aromatic protons of the two phenyl rings. The chemical shifts of H^{17}, H^8, and H^9 (δ = 7.82 and 7.60 ppm) represent characteristic downfield values of protons positioned ortho to the diazinyl moiety. Furthermore, the downfield shift of the singlet for H^{21} (7.18 ppm) and the upfield shift for H^{19} (8.11 ppm) indicate the presence of a hydroxyl group at the meta and ortho positions relative to these protons, respectively [34,35]. Finally, the resonance observed at 3.41 ppm was assigned to the methyl protons. The ^{13}C NMR spectrum of the azo-oxime ligand (H_2L, **1**) (Figure S6) displayed a range of distinct chemical shifts, supporting the proposed molecular structure. A resonance at 159.50 ppm was attributed to the carbon atom (C20) bonded to a hydroxyl group, while the oximatic carbon (C28) appeared at 145.46 ppm. The signals corresponding to carbons C2, C4, C14, and C15 (δ = 122.82, 122.71, 125.75, and 121.76 ppm) are characteristic of aromatic carbons linked to the azo (N=N) group, which is connected to C3 (δ = 150.50 ppm) and C13 (δ = 146.10 ppm). Additional peaks observed at 130.36, 141.37, 119.76, and 117.31 ppm were assigned to the aromatic carbons C1, C5, C6, C16, and C18, respectively. The signal at 21.46 ppm was attributed to the methyl carbon attached to the benzene ring.

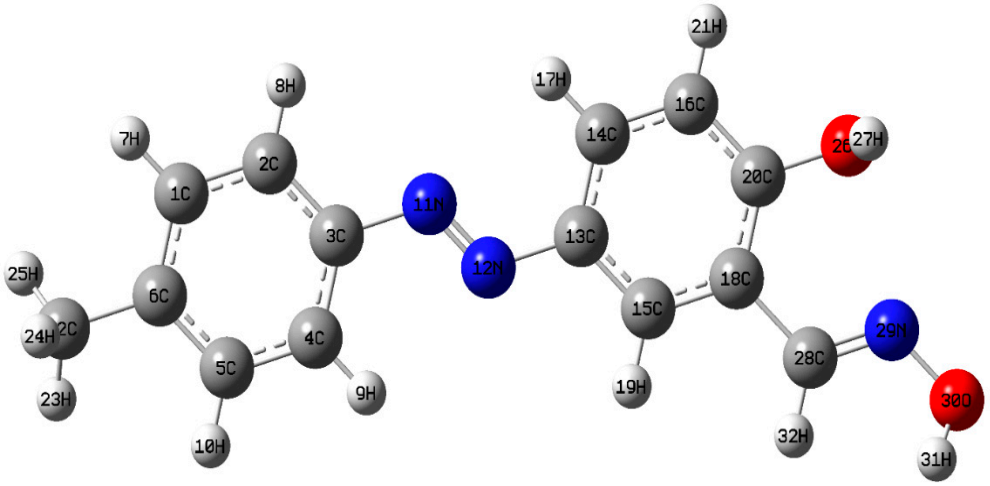

Figure 2. The optimized structure obtained for azo-oxime (H_2L, **1**) by DFT/B3LYP/(6-311G(d,p)).

2.2.3. Magnetic Moment and Electronic Absorption Spectroscopic (EAS) Measurements

The structure of the azo-oxime molecule contains multiple electron-donating sites, primarily the azo group (–N=N–), the oxime group (–CH=NOH), and the phenolic hydroxyl group (–OH). These functional groups possess lone pairs of electrons that can participate in chelation with metallic ions. The EAS of the ligand and its complexes in DMSO, along with the magnetic moment data of its solid complexes, are summarized in Table 1. The ligand spectrum exhibits three distinct absorption regions in the UV–visible range. The first set

of bands, appearing at 265 and 287 nm, can be attributed to $\pi \rightarrow \pi^*$ electronic transitions within the benzene ring and intra-ligand charge transfer transitions [36,37]. The second set of absorptions, observed at 297 nm and 341 nm, corresponds to $n \rightarrow \pi^*$ transitions related to the oxime moiety [37]. The third prominent band at 359 nm is attributed to a $\pi \rightarrow \pi^*$ transition involving the azo group electrons [36]. Additionally, a broader absorption band detected at 442 nm is allotted to a $\pi \rightarrow \pi^*$ transition that extends over the entire conjugated system, predominantly representing a charge transfer process from the phenolic moiety to the azo-oxime framework [36]. The spectra of the metallic complexes revealed a noticeable shift in the n–π^* transitions, which is likely attributed to the coordination of the phenolic and oximatic groups with the metallic cations. The VO^{2+} cation has a single electron in the d orbital, corresponding to the term symbol ^2D. In an ideal octahedral crystal field, this electron occupies the t_{2g}, resulting in a $^2T_{2g}$ ground state. Upon excitation this electron transferred to e_g orbital, giving rise to a single absorption band associated with the $^2T_{2g} \rightarrow {}^2E_g$ transition. However, because of the asymmetrical orientation of the V=O bond along one axis, the ideal octahedrally symmetry is reduced to rhombic (C_{2v}) or tetragonal (C_{4v}) symmetries, as the symmetry is further reduced. In the C_{4v} symmetry, the $^2T_{2g}$ level undergoes splitting into $^2B_2$ and ^2E states, while ^2E_g splits into $^2B_1$ and $^2A_1$. As a result, three electronic transitions are anticipated corresponding to bands in the ranges 900–725, 690–525, and 500–320 nm, which originate from $^2B_2$ ground state to the excited states (^2E, $^2B_1$, and $^2A_1$). If the symmetry is further reduced to C_{2v}, the ^2E level undergoes additional splitting into $^2B_1$ and $^2B_2$ sublevels, resulting in four observable bands [38,39]. For VO^{2+} complex (**2**), the EAS show off two characteristic bands at 686 and 944 nm ascribing to the transitions $^2B_{2g} \rightarrow {}^2B_{1g}(d_{xy} \rightarrow d_{x2-y2})$ and $^2B_{2g} \rightarrow {}^2E_g(d_{xy} \rightarrow d_{xz},d_{yz})$ correspondingly which is coherent with a tetragonal structure for the VO^{2+} ion (Figure 1a) [38–40]. The absence of additional observable transitions may be interfered with or overlapped by the intense bands associated with the azo groups, which correspond to $\pi \rightarrow \pi^*$ and charge-transfer transitions. The calculated magnetic moment (μ_{eff} of 1.65 BM) agrees well with the expected spin-only value for a single unpaired electron [40].

In an octahedral crystal field, the ground state of six-coordinated Cu^{2+} cation (d^9) is $t_{2g}{}^6e_g{}^3$ with ^2E_g term, while the excited state is $t_{2g}{}^5e_g{}^4$ with $^2T_{2g}$ term. Therefore, the $^2E_g \rightarrow {}^2T_{2g}$ is the expected electronic transition. However, the Jahn–Teller effect distorts the octahedral arrangement by either elongation or compression of the octahedron, leading to tetragonal symmetry where the $^2T_{2g}$ also splits into $^2B_{2g}(d_{xy})$ and $^2E_g(d_{xz},d_{yz})$ levels, while the ^2E_g is split into $^2B_{1g}(d_{x2-y2})$ and $^2A_{1g}(d_{z2})$ levels. Therefore, for tetragonal (D_{4h}) symmetry, three bands are expected viz. $^2B_{1g} \leftarrow {}^2A_{1g}$, $^2B_{1g} \leftarrow {}^2B_{2g}$, $^2B_{1g} \leftarrow {}^2E_g$, which may appear around 1000, 650, and 500 nm sequentially [38,39,41]. Observing these theoretical effects in practice is often challenging because interference and the small energy differences between d-orbital levels make resolving discrete peaks difficult. In the case of **Cu^{2+}** complexes (**3**,**4**) spectra disclosed a very broad band centered at 922 and 900 nm ascribable to $^2B_{1g} \leftarrow {}^2A_{1g}d_{z2}$ (ν_1) transitions and a shoulder at 485, 560 and 500, 575 nm ascribable to $^2B_{1g} \leftarrow {}^2B_{2g}(\nu_1)$ and $^2B_{1g} \leftarrow {}^2E_g$, transitions [39,42]. But for the Cu^{2+} complex (**5**) there are two weak bands at 457 and 550 nm allocated to $^2B_{1g} \leftarrow {}^2A_{1g}$, $^2B_{1g} \leftarrow {}^2B_{2g}$ transitions, and a shoulder centered at 940 nm ascribable to $^2B_{1g} \leftarrow {}^2B_{2g}(\nu_1)$, transition. These data indicate that they have distorted octahedral or square planer geometries (Figure 1a,b). The magnetic moment values of the solid **Cu^{2+}** complexes (**3**–**5**) at room temperature ranged from 1.67 to 1.88 BM, which is compatible with one unpaired electron system. The Fe^{3+} cation with $3d^5$ configuration has ^6S term symbol (S = 5/2, L = 0). In an ideal octahedral crystal field, these electrons occupy the t_{2g} and e_g orbitals in a high-spin configuration ($t_{2g}{}^3e_g{}^2$), resulting in a $^6A_{1g}$ ground state. Upon excitation, d-d electronic transitions happen from the $^6A_{1g}$ ground state to higher quartet states (S = 3/2) derived from electron within the d-manifold

($t_{2g}^3 e_g^2 \rightarrow t_{2g}^4 e_g^1$). The lowest such exciting states are $^4T_{1g}$ and $^4T_{2g}$ both of which in a strict symmetry are spin-forbidden ($\Delta S \neq 0$) and thus weak; however, coupling, spin–orbit effects, and symmetry distortion may render them noticeable. For the Fe^{3+} complex (**6**), the EAS displays two weak broad bands at 565 and 850 nm, which can be allotted to the transitions $(\nu_1)^6A_{1g}(S) \rightarrow {}^4T_{1g}(G)$ and $(\nu_2)^6A_{1g}(S) \rightarrow {}^4T_{2g}(G)$. These observations are coherent with a distorted octahedral geometry for Fe^{3+} ion (Figure 1c). The measured magnetic moment (μ_{eff} = 5.90 BM) matches well with the spin-only value expected for a high-spin Fe^{3+} ion containing five unpaired electrons.

Table 1. EAS of the azo-oxime ligand (H_2L, **1**) and its VO^{2+}, Cu^{2+}, and Fe^{3+} complexes (**1**–**6**).

Compound	Bands (nm) in DMSO	Electronic Transition	μ_{eff} (BM)	Geometry
Azo-oxime	254, 265, 287, 298, 341, 359, 442	$\pi \rightarrow \pi^*$, $n \rightarrow \pi^*$	—	
VO^{2+} complex (**2**)	260, 281, 384, 455, 686, 944	$^2B_{2g}(d_{xy}) \rightarrow {}^2E_g(d_{xz},d_{yz})(\nu_1)$, $^2B_{2g}(d_{xy}) \rightarrow {}^2B_{1g}(d_{x2-y2})(\nu_2)$	1.65	Distorted octahedral
Cu^{2+} complex (**3**)	255, 284, 335, 417, 440, 485, 560, 922	$^2B_{1g} \leftarrow {}^2E_g$ ($d_{x2-y2} \leftarrow d_{yz}d_{xz}$)	1.67	Distorted
Cu^{2+} complex (**4**)	256, 287, 332, 382, 439, 500, 575, 900	$^2B_{1g} \rightarrow {}^2A_{1g}$ ($d_{x2-y2} \leftarrow d_{z2}$)	1.71	octahedral
Cu^{2+} complex (**5**)	262, 280, 336, 376, 425, 457, 550, 940	$^2B_{1g} \rightarrow {}^2B_{2g}$ ($d_{x2-y2} \leftarrow d_{xy}$)	1.88	Square planar
Fe^{3+} complex (**6**)	260, 365, 412, 456, 565, 850	$(\nu_2)^6A_{1g}(S) \rightarrow {}^4T_{2g}(G)$ $(\nu_1)^6A_{1g}(S) \rightarrow {}^4T_{1g}(G)$	5.91	Distorted octahedral

2.2.4. Electron Spin Resonance (ESR) Spectrum of VO^{2+} and Cu^{2+} Complexes

Further details regarding the geometries of polycrystalline VO^{2+} and Cu^{2+} complexes are provided by their ESR spectra at 25 °C on the X-band (9.8 GHz). The data is recorded in Table 2.

VO^{2+} Complex ESR

The VO^{2+} complex (d^1, ^{51}V, I = 7/2) ESR shows eight hyperfine lines, which correspond to the expected 2I + 1 = 8 splitting from the ^{51}V nucleus confirming a mononuclear V^{4+} species with an axially anisotropic pattern ($g_\perp > g_{||}$ and $A_{||} >> A_\perp$) consistent with a distorted octahedral structure and a d_{xy} ground state [43]. Two sets of resonance components, parallel ($g_{||}$) and perpendicular ($g_\perp$), indicate axial symmetry. The absence of nitrogen super-hyperfine splitting suggests the interaction occurs mainly between the electron spin and the ligand [44]. These findings support a deformed octahedral structure for VO^{2+} [45,46]. The molecular orbital coefficients, α^2 and β^2, were calculated using standard equations (Equations (1) and (2)) [40].

$$\alpha^2 = \frac{\left(2.0023 - g_{\parallel}\right) Exy}{8\lambda\beta^2} \quad (1)$$

$$\beta^2 = \frac{7}{6}\left[\left(-\frac{A_{\parallel}}{P}\right) + \left(\frac{A_{\perp}}{P}\right) + \left(g_{\parallel} - \frac{5}{14}g_{\perp}\right) - \frac{9}{14}g_e\right] \quad (2)$$

where P = 128 × 10^{-4} cm^{-1}, λ = 135 cm^{-1} and E is the electronic transition energy of $^2B_2 \rightarrow {}^2E$. The higher β^2 value compared to α^2 indicates that in-plane π-bonding is less covalent than in-plane σ-bonding [40,47]. The β^2 value for the VO^{2+} complex is consistent with previously reported data for VO^{2+} complexes [46–50].

Cu^{2+} Complex ESR

The ESR spectra of Cu^{2+} complexes (**3**–**5**) exhibit anisotropic signals with $g_{\parallel}$ values of 2.232, 2.239, and 2.218; $g_{\perp}$ values of 2.037, 2.031, and 2.025; and g_{iso} values of 2.102, 2.100, and 2.090. These values are characteristic of d^9 systems with an axial symmetry corresponding to a $d_{(x^2-y^2)}$ ground state, which is typical for Cu^{2+} complexes [51,52]. The observed g-values suggest that complexes (**3**–**5**) adopt either octahedral or square-planar geometries [53,54]. The ESR data show $g_{\parallel} > g_{\perp} > 2.0023$, indicating a distorted environment around the Cu^{2+} ion [55]. The parameter G, defined as $G = (g_{\parallel} - 2)/(g_{\perp} - 2)$, provides information about exchange interactions [56]. When $G < 4.0$, significant exchange coupling occurs; when $G > 4.0$, the tetragonal axes are aligned parallel or only partially misaligned. For complexes (**3**–**5**), G values are 6.61, 8.27, and 9.32, indicating the presence of tetragonal axes. The ratio $g_{\parallel}/A_{\parallel}$ serves as a stereochemical diagnostic: values between 105 and 135 indicate a square-planar geometry, while values between 150 and 250 cm^{-1} suggest a tetragonally distorted octahedral geometry [57]. For complexes (**3**) and (**4**), $g_{\parallel}/A_{\parallel}$ values of 171.3 and 152.8 confirm tetragonally distorted octahedral structures, whereas complex (**5**) has a $g_{\parallel}/A_{\parallel}$ value of 133.8, consistent with a square-planar geometry [56,58]. According to Kivelson and Neiman, the $g_{\parallel}$ value also reflects the nature of the metal–ligand bonding: $g_{\parallel} > 2.3$ corresponds to predominantly ionic bonds, while $g_{\parallel} < 2.3$ indicates primarily covalent bonding [59]. Since all Cu^{2+} complexes (**3**–**5**) exhibit $g_{\parallel} < 2.3$, their Cu–ligand bonds are mainly covalent. Moreover, the g-values can be related to the parallel ($k_{\parallel}$) and perpendicular ($k\perp$) components of the orbital reduction factor (k) using established equations (Equations (3)–(5)) [60–63].

$$k_{\parallel}{}^2 = \left(g_{\parallel} - 2.0023\right)\Delta Exy/8\lambda^{\circ} \quad (3)$$

$$k_{\perp}{}^2 = \left(g_{\parallel} - 2.0023\right)\Delta Exz/2\lambda^{\circ} \quad (4)$$

$$k^2 = \left(k_{\parallel}{}^2 + 2k_{\perp}{}^2\right)/3 \quad (5)$$

Here, λ_0 is the spin–orbit coupling constant for the free Cu^{2+} ion (-828 cm^{-1}), while ΔE_{xy} and ΔE_{xz} correspond to the electronic transitions $^2B_{1g} \rightarrow {}^2E_g$ and $^2B_{1g} \rightarrow {}^2B_{2g}$, respectively. The values of $k_{\parallel}{}^2$, $k_{\perp}{}^2$, and k^2 indicate that $k_{\parallel}{}^2 < k^2$, confirming that the ground state of complexes (**3**) and (**4**) is $^2B_{1g}$. Furthermore, the orbital reduction factor k reflects the covalent or ionic nature of the Cu^{2+} environment: $k < 1$ corresponds to a predominantly covalent environment, whereas $k > 1$ indicates an ionic character. The K values for complexes (**3**–**5**) are 0.70, 0.662, and 0.634, respectively, all below unity, indicating a covalent environment consistent with the $g_{\parallel}$-value data [62–64]. The in-plane σ-bonding parameter, α^2, can be evaluated using the following equation (Equation (6)) [51,54].

$$\alpha^2 = \left(g_{\parallel} - 2.0023\right) + \frac{3}{7}(g_{\perp} - 2.0023) - \left(\frac{A_{\parallel}}{P}\right) + 0.04 \quad (6)$$

Here, P represents the free-ion dipolar parameter, equal to 0.036 cm^{-1}. If $\alpha^2 = 1$, the bond is purely ionic, whereas $\alpha^2 = 0.5$ corresponds to a purely covalent bond, assuming $P = 0.036$ cm^{-1} and $K = 0.43$ [51,54]. For Cu^{2+} complexes (**3**–**5**), the calculated α^2 values are 0.647, 0.696, and 0.726, indicating a predominantly covalent character for the in-plane σ-bonding [65]. The γ and β coefficients, which describe the out-of-plane and in-plane π-bonding contributions, respectively, can be evaluated using the following equations (Equations (7) and (8)) [60].

$$\alpha^2\gamma^2 = K_{\perp}{}^2 \quad (7)$$

$$\alpha^2\beta^2 = K_{\parallel}{}^2 \quad (8)$$

The Cu^{2+} complexes' (**3**–**5**) γ^2 values are 0.96, 0.89 and 0.82, while the β^2 values are 0.67, 0.50 and 0.42 successively, suggesting that the out-of-plane and in-plane π-bonding are covalency in natura [58,60].

Table 2. ESR parameters of VO^{2+} and Cu^{2+} complexes.

Complex No.	VO^{2+}	Cu^{2+}(3)	Cu^{2+}(4)	Cu^{2+}(5)
$g_{\parallel}$	1.915	2.232	2.239	2.218
$g_{\perp}$	1.974	2.037	2.031	2.025
g_{iso} (a)	1.954	2.102	2.100	2.090
$A_{\parallel} \times 10^{-4}$ (cm^{-1})	143.0	136	146	166
$A_{\perp} \times 10^{-4}$ (cm^{-1})	46.1	38.1	28.1	37.3
$A_{iso} \times 10^{-4}$ (cm^{-1})	79.1	68.7	65.4	78.1
$g_{\parallel}/A_{\parallel}$ (cm)	-	171.3	152.8	133.8
G (b)	-	6.62	8.27	9.32
ΔE_{xy} (cm^{-1})	10,593	17,857	17,391	18,181
ΔE_{xz} (cm^{-1})	-	20,618	20,000	21,881
$K_{\parallel}{}^2$	-	0.620	0.622	0.593
$K_{\perp}{}^2$	-	0.433	0.346	0.306
K^2		0.496	0.438	0.402
K^2	-	0.658	0.588	0.554
K	--	0.700	0.662	0.634
α^2	0.884	0.647	0.696	0.726
β^2	0.974	0.67	0.50	0.42
γ	-	0.96	0.89	0.82

[a] $g_{iso} = (2g_{\perp} + g_{\parallel})/3$, [b] $G = (g_{\parallel} - 2)/(g_{\perp} - 2)$.

2.2.5. Thermogravimetric Analysis

The thermogram showed several stages of breakdown between 30 and 523 °C, culminating in the formation of residues made of metal oxide. Table 3 illustrates the mass loss correlation between the calculated and recommended formulae. The TG behaviors confirmed that the complexes of VO^{2+}, Cu^{2+}, and Fe^{3+} disintegrate in three or four phases, which are explained as follows:

(i) The initial stage observed in the TGA curve of the Fe^{3+} complex occurred between the temper 50 and 130 °C, showing a loss of mass equal to 7.40% (calcd. 7.64%). This weight reduction is attributed to the removal of two hydrated water molecules.

(ii) The elimination of coordinated water molecules between 130 and 260 °C is the second stage shown in the TGA curves of VO^{2+}, Cu^{2+} and Fe^{3+} complexes. This is accompanied by a mass loss that ranges from 4.33% (calcd. 4.16%) to 7.99% (calcd. 7.93%). As indicated in Table 3, this weight reduction is ascribed to the release of one or two coordinated water molecules.

(iii) The third stage detected in the TGA curves of VO^{2+}, Cu^{2+} and Fe^{3+} complexes corresponds to the elimination of anions between 225 and 360 °C, accompanied by a loss of mass ranges from 21.44% (calcd. 21.32%) to 25,98% (calcd. 25.89%). This weight reduction is ascribed to the release of Cl^-, $NO_3{}^-$, OAc^- or $SO_4{}^{2-}$ anions, as presented in Table 3.

(iv) The final stage represents the complete decomposition of VO^{2+}, Cu^{2+} and Fe^{3+} complexes through the removal of the organic moiety, leading to the creation of metal oxide residues. This process happens between 360 and 523 °C accompanied by a mass loss ranging from 48.44% (calcd. 49.07%) to 54.81% (calcd. 55.29%).

Table 3. The thermogravimetric analysis (TG) of VO^{2+}, Cu^{2+}, and Fe^{3+} complexes.

No.	Step	Temp. Range °C	Weight Loss Found (Calcd)	Assignment	Composition of the Residue
VO^{2+} complex (**2**)	1st	155–250	7.99 (7.93)	Lose two molecules of coordinated water	$[(H_2L)VO(SO_4)]$
	2nd	250–350	21.44 (21.13)	Lose one sulphate ion (H_2SO_4)	$[(H_2L)VO]$
	3rd	350–435	49.39 (50.92)	Breakdown of the complex forming V_2O_5	V_2O_5
Cu^{2+} complex (**3**)	1st	155–245	7.73 (7.62)	Lose two molecules of coordinated water	$[(H_2L\ Cu(OAc)_2]$
	2nd	255–330	24.66 (25.14)	Lose two acetate ions (CH_3COO)	$[(H_2L\ Cu]$
	3rd	330–505	49.58 (50.43)	Breakdown the complex forming CuO	CuO
Cu^{2+} complex (**4**)	1st	145–230	7.14 (7.52)	Lose two molecules of coordinated water	$[(H_2L)Cu(NO_3)_2]$
	2nd	260–300	25.98 (25.89)	Lose two nitrate ions (HNO_3)	$[(H_2L)Cu]$
	3rd	310–410	49.11 (49.97)	Breakdown the complex forming CuO	CuO
Cu^{2+} complex (**5**)	1st	165–225	4.31 (4.16)	Lose one molecule of coordinated water	$[(H_2L)Cu(SO_4)]$
	2nd	235–320	22.24 (22.18)	Lose one sulphate ion (H_2SO_4)	$[(H_2L)Cu]$
	3rd	320–475	54.81 (55.29)	Breakdown the complex forming CuO	CuO
Fe^{3+} complex (**6**)	1st	50–130	7.40 (7.64)	Lose two molecules of hydrated water	$[(L)FeCl_3(H_2O)]$
	2nd	130–225	3.33 (3.82)	Lose one molecule of coordinated water	$[(L)FeCl_3]$
	3rd	225–360	22.01 (22.56)	Lose three chloride ions (3HCl)	[(L)Fe]
	4th	360–523	48.44 (49.05)	Breakdown of the complex forming Fe_2O_3	Fe_2O_3

2.3. Molecular Modeling

2.3.1. Optimization of Geometry

Figures 2, S7 and S8 showed the ideal geometries of the azo-oxime (H_2L, **1**) and its VO^{2+}, Cu^{2+}, and Fe^{3+} complexes. The selected bond lengths and angle values for azo-oxime (H_2L, **1**) and its VO^{2+}, Cu^{2+}, and Fe^{3+} complexes (Table S1) verified that the VO^{2+}, Cu^{2+}, and Fe^{3+} complexes have a hexa-chelated arrangement, where the azo-oxime chelator (H_2L, **1**) connects the VO^{2+}, Cu^{2+}, and Fe^{3+} ions via oximatic nitrogen of protonated oxime group and protonated phenolic oxygen atoms. The data on bond lengths discovered a slight shortening in the length of the $^{28}C{=}N^{29}$ bond and an elongation of the bond lengths $^{30}C\text{-}O^{26}$ in complexes, confirming that these bonds participate in linking with VO^{2+}, Cu^{2+}, and Fe^{3+} centers. In the optimum structures of VO^{2+}, Cu^{2+}, and Fe^{3+} complexes, the bond length between the oximatic nitrogen and the phenolic oxygen atoms with VO^{2+}, Cu^{2+}, and Fe^{3+} cations is found to range from 2.75 to 2.80 A°. The bond length between protonated phenolic oxygen atoms with VO^{2+}, Cu^{2+}, and Fe^{3+} cations is found to range from 2.71 to 2.77 A°. In hexa-coordinated Cu^{2+}(**3**,**4**) complexes, the four equatorial positions were populated by phenolic oxygen, oximatic nitrogen atoms, and water molecules, while the two axial locations were inhabited by two acetate or nitrate anions. In the case of VO^{2+}, the complex has four equatorial sites, which are occupied by an oximatic nitrogen atom, a phenolic oxygen atom, a water molecule, and sulfate anions, while the two axial locations were occupied by the water molecule and the vanadyl oxygen. In the Fe^{3+} complex, the four equatorial sites were occupied by oximatic nitrogen atoms, a phenolic oxygen atom, a water molecule, and a chloride anion, whereas the two axial locations were occupied by

chloride ions. In the tetra-coordinated **Cu^{2+}** complex (**5**), the four-square sites are occupied by a oximatic nitrogen atom, phenolic oxygen atom, water molecule, and sulfate anion. The geometry of this four-coordinate complex was evaluated using the geometric index τ_4 estimated by $\tau_4 = 360^\circ - (a + b)/141^\circ$, whereas b and α are the two largest valence angles of the chelation center. The literature states that the τ_4 values equal 0 for square planar geometry and the τ_4 values equal 1 for tetrahedral geometry. In contrast, the range for intermediate geometry, which includes seesaw and trigonal pyramidal shapes, is 0 to 1. The τ_4 value for the tetra-coordinate **Cu^{2+}** complex (**5**) is equal to 0.0497. This conclusion proves that the **Cu^{2+}** complex (**5**) has a predominantly square planar structure [66,67].

2.3.2. Molecular Parameters

The quantum chemical properties of the organic and organometallic compounds, such as the energies of the lowest unoccupied molecular orbital (ELUMO) and the highest occupied molecular orbital (EHOMO), were ascertained using computational computations. These parameters were computed using the following formulas (Equations (9)–(15)), and Table 4 presents the findings [68–70].

$$\text{Ionization potential (I)} = -E_{HOMO} \tag{9}$$

$$\text{Electron affinity (A)} = -E_{LUMO} \tag{10}$$

$$\Delta E_{gap}\ \text{(Energy gap)} = E_{LUMO} - E_{HOMO} \tag{11}$$

$$\text{(Electronegativity)}\ \chi = -\frac{E_{LUMO} + E_{HOMO}}{2} \tag{12}$$

$$\eta\text{(hardness)} = \frac{E_{LUMO} - E_{HOMO}}{2} \tag{13}$$

$$\sigma\text{(softness)} = \frac{1}{\eta} \tag{14}$$

$$\text{(Reactivity index)}\ \Delta N_{max} = -\frac{\mu}{\eta} \tag{15}$$

A molecule's ability to donate and take electrons is reflected in the E_{HOMO} and E_{LUMO} quantum chemical descriptors, respectively. Frontier molecular orbital (FMO) theory states that interactions between the HOMO and LUMO of interacting species have a major role in determining chemical reactivity. Larger electron-donating capacity toward acceptors, such as metal cations with empty orbitals, is indicated by a larger E_{HOMO}, whereas higher electron-accepting potential is indicated by a lower E_{LUMO}. For the azo-oxime (**H_2L**, **1**), the calculated **E_{HOMO}** is comparatively high, signifying a substantial electron donation to the empty d-orbitals of **Cu^{2+}**, **VO^{2+}** and **Fe^{3+}**, and accordingly favorable chelation. The intrinsic stability of the compounds is confirmed by the negative orbital energies of the HOMO, LUMO, and nearby orbitals. According to orbital analysis, the LUMO is widely delocalized over the whole molecule, whereas the HOMO is primarily localized on the azo group with little contributions from the phenyl and toluene carbon atoms (Figure 3). The distribution of LUMO and HOMO iso-densities VO^{2+}, Cu^{2+}, and Fe^{3+} complexes is nearly identical in all complexes. HOMO is dispersed on the azo linkage, involving some carbon atoms of toluene and phenyl or on a coordination center involving coordinated atoms, while LUMO is spread on the azo moiety, involving the phenyl and toluene carbon atoms or on chelation sites (Figures S7–S12). The HOMO-LUMO energy gap (ΔE_{gap}), a crucial molecular stability indicator, can be used to build a theoretical model for evaluating structural and conformational stability in molecular systems. The comparatively high energy gap of azo-oxime (H_2L), (ΔE_{gap} = 3.66) signifies a strong inherent stability and a favorable tendency to chelate with Cu^{2+}, VO^{2+} and Fe^{3+} cations. On the other

hand, compared to the free ligand, the resultant Cu^{2+}, VO^{2+} and Fe^{3+} complexes show lower energy gaps (ΔE_{gap} = 2.10–3.06 eV, Table 4), indicating higher chemical reactivity and decreased stability. These findings are corroborated by global reactivity descriptors. Among the compounds under study, azo-oxime has the highest ionization potential (IP) and lowest electron affinity (EA), which are derived from HOMO and LUMO energies. This indicates greater resistance to oxidation and a lesser propensity to take electrons. On the other hand, the Cu^{2+}, VO^{2+} and Fe^{3+} complexes show higher EAs and lower IPs, which are in line with increased reactivity. The chemical stability and reactivity can also correlate to absolute hardness (η) and absolute softness (σ). The free ligand is the hardest species (1.83 eV) while the Cu^{2+}, VO^{2+} and Fe^{3+} complexes are softer (η = 1.80–1.01 eV, σ = 0.56–0.99 eV (Table 4), proving that metallic chelation improves the reactivity of azo-oxime (H_2L) and reduces its hardness. These results are completely in line with the patterns shown in the global reactivity descriptors and HOMO-LUMO gaps.

$$\eta \text{ (hardness)} = \frac{E_{LUMO} - E_{HOMO}}{2} \tag{16}$$

$$\sigma \text{ (softness)} = \frac{1}{\eta} \tag{17}$$

In complexation systems, the metal cation is a Lewis acid and the chelator is a Lewis base. Chelators with soft base character are very good at creating stable complexes because metal cations are regarded as soft acids. As a result, chelators with appropriate global softness (σ) values have a strong tendency to coordinate effectively with metal cations. The ligand's chemical potential (μ) provides more evidence for this behavior. As illustrated in Table 4, The azo-oxime has the largest chemical potential (μ = −4.13 eV), suggesting a strong propensity to interact with metallic cations.

$$\mu \text{ (Chemical potentials)} = -\chi \tag{18}$$

The stabilizing energy that a system obtains when it receives an extra electronic charge from its environment is measured by ΔN_{max}. The chemical potential (μ) of the molecule determines the strength and direction of this charge transfer. When an electrophile acquires an electronic charge, it stabilizes itself by reducing its energy. As a result, an electrophilic species' chemical potential is negative, which is in line with the values shown in Table 4.

$$\text{(Reactivity index) } \Delta N_{max} = -\frac{\mu}{\eta} \tag{19}$$

Based on μ and η, Parr et al. proposed the concept of electrophilicity index (ω, Equation (20)) [71,72], where a lower ω reflects greater nucleophilic character. The azo-oxime ligand H_2L shows the lowest ω (4.65 eV) among the series, consistent with its nucleophilic character, while the VO^{2+}, Cu^{2+}, and Fe^{3+} complexes show markedly higher values (4.87–14.29 eV, Table 4), indicating that metal coordination substantially reduces the ligand's nucleophilicity.

$$\text{(Electrophilicity index) } \omega = \frac{\mu^2}{2\eta} = \frac{(IP + IA)^2}{4(IP - IA)} \tag{20}$$

In order to provide a more thorough assessment of a system's electrophilic behavior, Gázquez et al. developed the parameters of electro-donating power (ω^-, Equation (21)) and electro-accepting power (ω^+, Equation (22)), which are comparable to the electrophilic index (ω) [73]. Chattaraj et al. [74]] followed by comparing ω^- and ω^+ using the notion of net electrophilicity ($\omega^{\pm}$, Equation (23)) [74]. These parameters reflect the overall tendency

of a system to accept electrons in relative to its capability to provide them. The electrophilic and nucleophilic descriptors obtained from DFT can be used to evaluate the reactivity trends of the azo-oxime (H_2L) and its Cu^{2+}, VO^{2+} and Fe^{3+} complexes based on the quantum chemical parameters in Table 4. The HOMO and LUMO energies illustrate that coordination with metallic ions typically results in lower orbital energies than those of the free ligand, indicating less reactivity and increased molecule stability. The energy gap (ΔE) gradually dropped from 3.66 eV for azo-oxime to 2.01 eV for the Fe^{3+} complex, recommending that Fe^{3+} improves electron delocalization and charge transfer interactions, which can increase the reactivity of substance. This trend is further supported by the electrophilic index (ω) and associated parameters (ω^+ and ω^-). The azo-oxime (H_2L, **1**) has the lowest $\omega^{\pm}$ value (9.77 eV), whereas the Fe^{3+} complex has the highest $\omega^{\pm}$ value (28.84 eV), implying the most electrophilic property. This suggests that the molecules' capacity to receive electrons is much improved by metal coordination, especially with Fe^{3+}. Additionally, the electro-accepting power (ω^+) increases remarkably from 2.82 eV (H_2L) to 11.74 eV (Fe^{3+}). Concurrently, the electro-donating power (ω^-) rises from 6.95 eV to 17.10 eV, implying that chelation improves both electron donation and acceptance capacities.

$$(\text{Electron accepting power})\ \omega^+ = \frac{(\text{IP} + 3\text{EA})^2}{16(\text{IP} - \text{EA})} = \frac{(E_{HOMO} + 3E_{LUMO})^2}{16(E_{LUMO} - E_{HOMO})} \quad (21)$$

$$(\text{Electron donating power})\ \omega^- = \frac{(3\text{IP} + \text{EA})^2}{16(\text{IP} - \text{EA})} = \frac{(3E_{HOMO} + E_{LUMO})^2}{16(E_{LUMO} - E_{HOMO})} \quad (22)$$

$$(\text{Net Electrophilicity})\ \omega^{\pm} = \omega^- + \omega^+ \quad (23)$$

Domingo et al. [75] developed the nucleophilic index (N_{Nu}, Equation (24)), which quantifies a system's nucleophilic ability based on the energy of the highest occupied molecular orbital (HOMO) obtained from DFT calculations, as opposed to the electrophilic index (ω). Here, E_{HOMO}^{TCE} and E_{HOMO}^{Nu} denote to the HOMO energies of the tetracyanoethylene (TCE, −8 eV) and nucleophile correspondingly. The estimated quantum chemical parameters in Table 4 offer important information about the electrophilic and nucleophilic properties of azo-oxime and its VO^{2+}, Cu^{2+}, and Fe^{3+} complexes. According to Kiyooka's intrinsic reactivity index (IRI), Domingo's nucleophilic index ($\mathbf{N_{Nu}}$) and related electrophilicity index (ω), discrete tendencies in reactivity can be noted on chelation. The free azo-oxime (H_2L) has E_{HOMO} of 5.96 eV, with a moderate nucleophilic index (N_{Nu}) equal to 2.04 eV and IRI of 2.25 eV, implying balanced electron-accepting and -donating capabilities. Upon chelation with metallic ions, the energy gap (ΔE) gradually decreases (from 3.66 eV for azo-oxime (H_2L) to 2.01 eV for Fe^{3+} complex), and reflects improved electronic delocalization and increased chemical softness (σ). The VO^{2+}, Cu^{2+}, and Fe^{3+} complexes show comparable electronic characteristics, with E_{HOMO} ranged from −5.98 to −6.37 eV and $\mathbf{N_{Nu}}$ ranged from 2.02 to 1.63 eV correspondingly, signifying comparatively stable and moderately nucleophilic species. The $\mathbf{Cu^{2+}}$ complex shows higher IRI (5.33 eV) and a lower $\mathbf{N_{Nu}}$ (1.63 eV), implying improved electrophilic character due to intense ligand–metal interactions. Among all synthetics, the Fe^{3+} complex exhibits the lowest ΔE (2.01 eV), the highest IRI (5.33), and the highest electrophilicity index (ω = 14.29 eV), signifying strong chemical reactivity and electrophilic behavior.

$$N_{Nu} = E_{HOMO}^{Nu} - E_{HOMO}^{TCE} \quad (24)$$

The high softness (σ) and chemical potential (μ) values for $\mathbf{Fe^{3+}}$ complex are further confirmed by its strong electron-accepting tendency. This is coherent with concept of Ayers electrofugality, which states that the enhanced leaving-group capability is correlated with higher electron affinity (EA) and ionization potential (IP). Overall, it is evident from the

trend of N_{Nu} (Fe^{3+} < Cu^{2+}(**5**) < Cu^{2+}(**4**) < Cu^{2+}(**3**) < VO^{2+} < H_2L) and the inverse trend of **ω** Fe^{3+} > Cu^{2+}(**5**) > Cu^{2+}(**4**) > Cu^{2+}(**3**) > VO^{2+} > H_2L clearly demonstrate that metallic chelation significantly increases the azo-oxime's electrophilic nature, with Fe^{3+} complex being the most reactive and electron-deficient species.

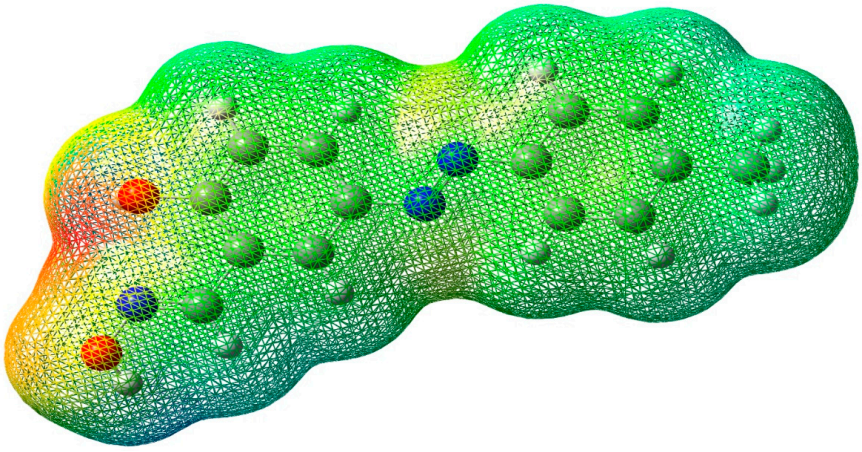

Figure 3. Molecular electrostatic potential of the azo-oxime (H_2L, **1**) by DFT/B3LYP/(6-311G(d,p)).

To simultaneously describe the nucleophilic and electrophilic behaviors with a single parameter, Kiyooka et al. [76] suggested the intrinsic reactivity index (IRI) as a standard measure of chemical activity. Moreover, Ayers et al. [77] suggested additional two reactivity indices nucleofugality (ΔE_n) and electrofugality (ΔE_e) that can be employed to forecast the leaving groups' behavior through chemical reactions. These indices show that a leaving group's electron-donating (escape) and electron-accepting properties can be assessed using its ionization potential (IP) and electron affinity (EA) (Equations (25)–(27)). According to the information shown in Table 4, the electron affinity (EA) values rise from 2.30 to 4.36 eV, while the ionization potential (IP) values range from 5.96 to 6.37 eV.

Computational analysis identifies the Fe^{3+} complex as the most chemically active species among the studied compounds. Specifically, it exhibits the highest ionization potential (**I**) and electron affinity (**A**), which, according to Ayers' interpretation, characterizes it as both an exceptional nucleofuge (exhibiting extreme electron-accepting capability) and a strong electrofuge (exhibiting higher electron-donating ability on detachable). This behavior is further substantiated by its significantly high electrophilicity index ω = 14.29 eV) and intrinsic reactivity index (IRI = 5.33 eV), highlighting a pronounced propensity for electron transfer processes. In contrast, the free azo-oxime ligand displays the lowest values for I, A, and ΔE_e, reflecting its weaker leaving-group character and greater kinetic stability. The established trend for ionization potential, electron affinity, and electrophilicity follows the order: **Fe^{3+} > Cu^{2+}(5) > Cu^{2+}(4) > Cu^{2+}(3) > VO^{2+} > H_2L**. This hierarchy confirms that metal coordination—particularly with Fe^{3+} —drastically reduces the energy gap (ΔE = 2.01 eV), thereby transforming the azo-oxime into a highly reactive and electron-responsive system.

The reactivity descriptors derived from the data disclose a consistent pattern in electrical behavior throughout the azo-oxime and its metallic complexes. The IRI rises noticeably on metallic coordination, going from 2.25 eV for azo-oxime to remarkably higher values in the complexes, especially the Fe^{3+} complex, which has the greatest IRI (5.33 eV), indicating stronger electronic polarization and increased overall reactivity on metallic binding. The ΔE_e displays a similar upward pattern, rising from 8.29 eV for azo-oxime to 13.51 eV for the Fe^{3+} complex, demonstrating that the chelation of Fe^{3+} notably stabilizes electron removal operations. On the other hand, the ΔE_n still relatively low for azo-oxime and its VO^{2+} and Cu^{2+} complexes (0.030, 0.048, 0.059, 0.097 and 0.396 eV) while increasing to

2.79 eV for the Fe^{3+} complex. This sharply enhancement reveals that Fe^{3+}complex has a great resistance to nuclear attacks in comparison to other ions. Overall, the data show that metallic coordination increases both nucleophilic and electrophilic stability, with Fe^{3+} creating the least reactive and most electronically robust and complex in the series.

$$\Delta E_e = \frac{(3IP - EA)^2}{8(I - A)} = \frac{(2\eta + \mu)^2}{4\eta} \quad (25)$$

$$\Delta E_n = \frac{(3EA - IP)^2}{8(IP - EA)} = \frac{(2\eta - \mu)^2}{4\eta} \quad (26)$$

$$IRI = \frac{IP + EA}{IP - EA} \quad (27)$$

Table 4. The calculated quantum chemical parameters of azo-oxime and its VO^{2+}, Cu^{2+}, and Fe^{3+} complexes by DFT/B3LYP/(6-311G(d,p)).

Compounds	H_2L	VO^{2+}(2)	Cu^{2+}(3)	Cu^{2+}(4)	Cu^{2+}(5)	Fe^{3+}(6)
E_{HOMO} (eV)	−5.96	−5.98	−5.99	−6.11	−6.31	−6.37
IP (eV)	5.96	5.98	5.99	6.11	6.31	6.37
E_{LUMO} (eV)	−2.30	−2.38	−2.43	−2.51	−3.16	−4.36
EA (eV)	2.30	2.38	2.43	2.51	3.16	4.36
ΔE (eV)	3.66	3.60	3.56	3.60	3.15	2.01
c (eV)	4.13	4.18	4.21	4.31	4.73	5.36
η (eV)	1.83	1.80	1.78	1.80	1.58	1.01
σ (eV^{-1})	0.55	0.56	0.56	0.56	0.63	0.99
μ (eV)	−4.13	−4.18	−4.21	−4.31	−4.73	−5.36
ω (eV)	4.65	4.87	4.98	5.17	7.11	14.29
s (eV^{-1})	0.27	0.28	0.28	0.28	0.32	0.50
N_{max}	2.25	2.33	2.37	2.40	3.00	5.33
ω^+ (eV)	2.82	3.00	3.09	3.40	4.94	11.74
ω^- (eV)	6.95	7.18	7.30	7.72	9.67	17.10
$\omega^\pm$ (eV)	9.77	10.18	10.40	11.12	14.60	28.84
N_{Nu} (eV)	2.04	2.02	2.01	1.92	1.69	1.63
IRI (eV)	2.25	2.33	2.37	2.47	3.00	5.33
ΔEe (eV)	8.29	8.41	8.47	8.74	9.86	13.51
ΔEn (eV)	0.030	0.048	0.059	0.097	0.396	2.790
Total energy (a.u.)	−856.1	−2727.3	−3106.5	−3210.0	3272.1	3576.9
Dipole moment	4.37	26.34	6.13	4.89	19.80	12.58

In addition, the energetic properties of synthesized compounds were estimated using DFT calculations at the B3LYP/6-311G(d,p) level, and the results are presented in Table 4. The calculated total energies clearly demonstrate that the predicted metallic complexes are energetically more stable than the parent azo-oxime (H_2L), indicating that complex formation is thermodynamically favorable. This enhanced stability can be attributed to strong metal–ligand interactions arising from effective coordination between the donor sites of the azo-oxime ligand and the metal cations. Moreover, the dipole moments of the complexes (6.13 and 26.34 Debye) are significantly higher than that of the parent azo-oxime (4.37 Debye), reflecting substantial charge redistribution and increased polarization upon chelation. These results highlight the pronounced effect of metallic coordination on the stability and electronic structure of the resulting complexes.

2.3.3. Molecular Electrostatic Potential (MEP)

MEP maps (Figures 3 and S15–S19) were generated using DFT calculations to analyze the charge distribution and regions of variable electrostatic potential in the ground state. The molecular electrostatic potential, $V(r)$, is defined by the following expression.

$$V(r) = \sum_{A} \frac{Z_A}{R_A - r} \int \frac{\rho(r')}{(r' - r)} d(r') \quad (28)$$

where Z_A is the nuclear charge of an atom A, R_A represents the position of the nucleus A, and r denotes the point in space at which the potential is evaluated. The function $\rho(r')$ corresponds to the electron density at the point r', which serves as a dummy integration variable over the entire molecular electron density [78]. This expression enables simultaneous consideration of nuclear attraction and electronic repulsion effects, providing a comprehensive description of the molecular charge environment. The resulting MEP surfaces were visualized using color-coded maps (Figures 4 and S15–S19), in which the electrostatic potential varies from negative (red, orange, and yellow) to positive (blue), with green regions corresponding to near-neutral potential. Regions of negative potential indicate high electron density and are therefore associated with nucleophilic behavior, while positive potential regions represent electron-deficient sites susceptible to electrophilic attack. As such, MEP analysis serves as a reliable predictor of reactive sites and preferred coordination centers within the molecular structure.

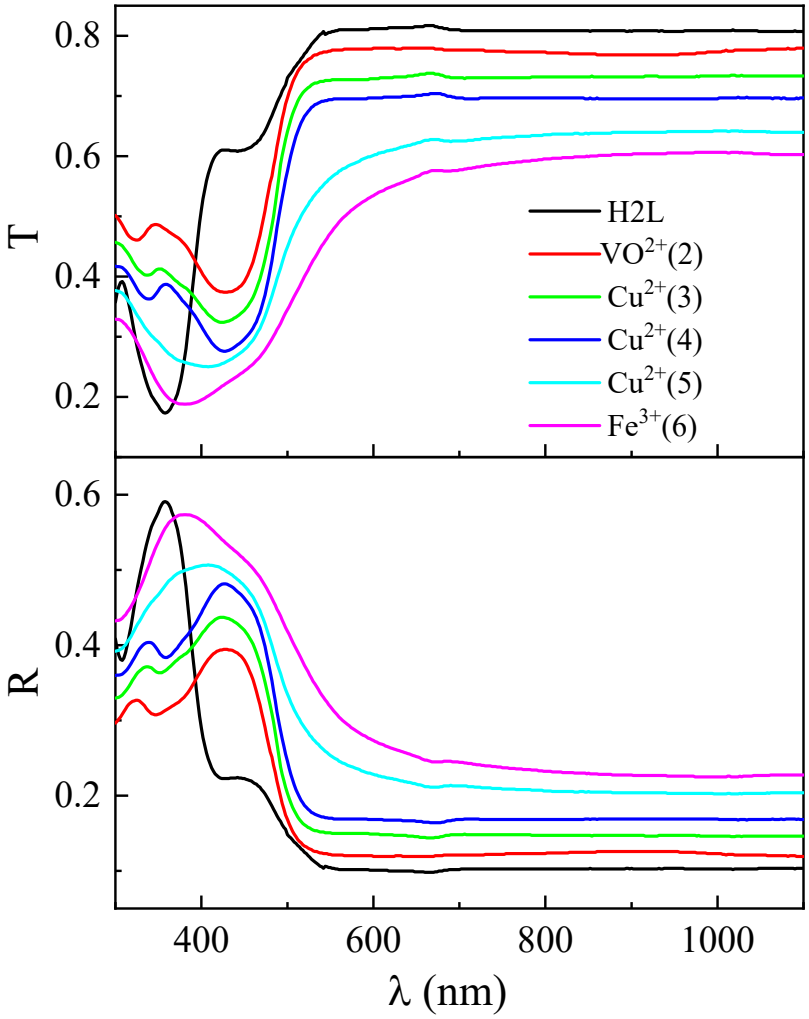

Figure 4. T and R spectra for the azo-oxime and its complex films.

For the azo-oxime (H_2L), the MEP map (Figure 4) reveals that the most negative electrostatic potential is localized around the oxygen atoms of the phenolic and oximatic functionalities, reflecting their strong electron-donating character. In contrast, carbon and hydrogen atoms predominantly exhibit neutral to positive potential regions. The accu-

mulation of negative charge density on these oxygen atoms identifies them as the most favorable coordination sites for metal ions [79,80]. This electronic distribution supports the experimentally observed coordination behavior toward VO^{2+}, Cu^{2+}, and Fe^{3+} cations and significantly influences charge redistribution, polarization, and charge-transfer processes, thereby modulating the optical absorption characteristics and dielectric properties of the ligand and its metal complex films relevant to photovoltaic performance. From an electronic-structure perspective, the MEP distribution is closely correlated with the frontier molecular orbital (FMO) characteristics and optical response of the system. Electron-rich regions contribute significantly to nonbonding (n) and π orbitals, which participate in $\pi \rightarrow \pi^*$ and $n \rightarrow \pi^*$ transitions observed in the UV–Vis spectra. Upon complexation, the negative potential regions—particularly those associated with oxygen donor atoms—facilitate efficient charge-transfer interactions between the ligand and metal centers. These interactions lead to enhanced electronic delocalization and reduced HOMO–LUMO energy gaps, which are commonly manifested as bathochromic (red) shifts in absorption maxima. Conversely, electron-deficient (blue) regions indicate sites that may stabilize excited-state electron density, impacting the molecule's light absorption intensity and optical band gap. In the VO^{2+}, Cu^{2+}, and Fe^{3+} complexes, the overall positive electrostatic potential favors metal-to-ligand charge transfer (MLCT), in agreement with the optical transitions observed in the UV–Vis spectra. The correspondence between molecular electrostatic potential (MEP) regions and electron-donating and electron-accepting sites accounts for the enhanced electronic delocalization within these systems, which in turn induces shifts in absorption wavelengths and modifies the optical response. Accordingly, MEP analysis serves not only to identify reactive regions but also to elucidate the relationship between molecular charge distribution and optical behavior, thereby linking quantum chemical features with spectroscopic properties.

2.3.4. Natural Bond Orbital (NBO) Analysis

NBO analysis offers a practical framework for researching charge transfer and conjugative effects in molecular systems and is a useful tool for analyzing intra- and intermolecular bonding as well as interactions between bonds [79,81–83]. Different donor–acceptor interactions and the accompanying stabilization energies inside the NBO basis were assessed using the second-order Fock matrix [79,84]. In these interactions, the electron density delocalizes from a donor (filled) NBO, which corresponds to the localized orbitals of the idealized Lewis structure, into an acceptor (empty) non-Lewis orbital. The stabilization energy, E(2), linked to electron delocalization between each acceptor NBO(j) and donor NBO(i) is computed as:

$$E^{(2)} = \Delta E_{ij} = qi\frac{F^2(\mathrm{ij})}{\varepsilon\mathrm{j} - \varepsilon\mathrm{i}} \quad (29)$$

where F_{ij} is the Fock matrix element between the natural bonding orbitals, q_i is the donor-orbital occupancy, and ε_j and ε_i are diagonal elements of orbital energies. The magnitude of the stabilization energy E(2) reflects the strength of interaction between electron donors and acceptors: higher E(2) values signify strong donor-to-acceptor interactions and a greater degree of conjugation in the system. The NBO 3.1 program developed in Gaussian 09 was used to calculate the azo-oxime's NBO at the DFT/B3LYP/6-311G(d,p) level of theory [85]. This analysis was achieved to examine electron-density delocalization, rehybridization, and intramolecular interactions within the molecule, with the results summarized in Table S3. Second-order perturbation theory was used to calculate stabilization energies in order to investigate intramolecular interactions in more detail. Table S4 displays the specific findings from this second-order perturbation analysis of the Fock matrix at the B3LYP/6-311G(d,p) level for azo-oxime. Stabilization energies greater than 3 kcal/mol have been selected

for Table S4. The main hyper-conjugative and $\pi \rightarrow \pi^*$ interactions stabilizing the ligand are highlighted by this second-order perturbation analysis (Table S4). The substantial delocalization within the ring is reflected in the usual contribution of 15–25 kcal/mol from the aromatic $\pi \rightarrow \pi^*$ interactions between adjacent C–C bonds. Strong intramolecular hyper-conjugative interactions between electrons in the azo-oxime molecule result in higher energy contributions from C^2-$C^3 \rightarrow C^1$-C^6 (17.43 kcal/mol), C^4-C^5 (20.73 kcal/mol); C^1-$C^6 \rightarrow C^2$-C^3 (22.81 kcal/mol) C^4-C^5(17.56 kcal/mol); C^4-$C^5 \rightarrow C^1$-C^6 (23.42 kcal/mol), C^2-C^3 (19.33 kcal/mol); C^{13}-$C^{15} \rightarrow N^{11}$-$N^{12}$(15.03 kcal/mol), C^{14}-C^{16}(20.40 kcal/mol), C^{18}-C^{20}(19.29 kcal/mol); C^{18}-C20$\rightarrow C^{13}$-C^{15}(21.76 kcal/mol), C^{14}-C^{16}(17.12 kcal/mol), C^{28}-N^{29}(11.47 kcal/mol); C^{14}-$C^{16} \rightarrow C^{13}$-$C^{15}$ (19.67 kcal/mol), C^{18}-C^{20} (22.70 kcal/mol). These interactions strengthen the aromatic system's conjugated structure. Remarkably, the π orbitals of the azo group (N^{11}=N^{12}) and the π^* orbitals of the nearby C-N and aromatic bonds exhibit the strongest hyper-conjugative effects, with stabilization energies as high as 30–36 kcal/mol, suggesting widespread resonance delocalization throughout the N=N and nearby π systems. Significantly, N^{11}-N^{12} contribute to the antibonding orbitals of nearby π-bonds of C^{13}–$C^{15}p^*$ and C^2–C^3p^* with stabilization energies 36.51 and 30.07 kcal/mol, correspondingly denoting to considerable resonance delocalization through the azo linkage ^{11}N=N^{12} and nearby π bonds. The electron richness of the oxime moiety is further enhanced by lone-pair$\rightarrow\pi^*$ interactions of O^{26} and O^{30} donating into π^*-orbitals of adjacent ^{18}C=C^{20} and ^{28}C=N^{29} bonds, which contribute significantly by 4.37 and 20.56 kcal/mol. Additionally, lone-pair$\rightarrow\pi^*$ interactions of O^{26} and O^{30} donating into π^*-orbitals of adjacent ^{16}C=C^{20}, ^{18}C=C^{20}, and ^{28}C=N^{29} bonds. The strong electronic connection between the oxime moiety and the aromatic moiety is confirmed by the very substantial stabilization of πC^{28}–$N^{29} \rightarrow \pi^* C^{18}$–$C^{20}$, which was equal to 72.18 kcal/mol.

The azo-oxime chelator's delocalization patterns and electronic structure are deeply revealed by the NBO analysis. The analysis of the σ-bond framework reveals that the aromatic C-C bonds are characterized by nearly symmetrical electron sharing between the two bonded carbons, with each atom contributing between 48.63 and 51.37% to the σ-bond and corresponding hybridizations ranging from $sp^{1.63}$ to $sp^{1.85}$ consistent with planar aromatic systems. This approves that the phenyl ring retains a high degree of resonance stabilization. The aromatic C–H bonds show the expected sp^2-carbon/high-s-character-hydrogen pattern, consistent with the σ-framework described above. The strong dominated p-nature of the N^{11}=N^{12} bond which is necessary for charge delocalization through the chelator molecule, is confirmed by the substantial p character on both nitrogen atoms in the azo-linkage (99.76% p in the π component). Moreover, the adjacent C-N bonds (C^3–N^{11} and N^{12}–C^{13}) display hybridizations equal to $sp^{2.79}$, $sp^{2.18}$, $sp^{2.21}$, and $sp^{2.76}$ for the four atoms respectively, signifying partial double-bond character because of π-electron donation from the phenyl ring and back-donation toward the azo unit. This delocalization is furthest demonstrated by the σ-framework polarization, in which the nitrogen atoms tend to have a greater contribution percentage (~59–60%) in the σ-bonds, reflective to its larger electronegativity and role as an electron-dense center.

The phenolic and oxime functional groups exhibit strong donor ability and electronic localization. The phenolic O–H bond on O^{26} displays highly p-character (80.76%) on oxygen. The O^{26} lone pairs show markedly unlike hybridization: LP1 is almost purely p-type (99.88% p-character, only 0.07% s), while LP2 is far more hybridized, with 50.90% s-character and 49.06% p-character. On the oxime oxygen O^{30}, the O–H bond likewise shows strong p-character on oxygen (78.82%), consistent with a highly polarized O–H σ-bond. The lone pairs on O^{30} display a hybridization pattern opposite that of O^{26}: LP1 is the more hybridized lone pair (51.46% s, 48.51% p), while LP2 is almost purely p-type (97.43% p, only 2.52% s). Second-order perturbation analysis shows that O^{30}'s resonance-active lone

pair coincides with its p-rich lone pair: LP2 donates strongly into the C^{28}–N^{29} π* orbital (E(2) = 20.56 kcal/mol), while the hybridized LP1 donates only weakly into the C^{28}–N^{29} σ* orbital (E(2) = 6.09 kcal/mol), confirming LP2 as the dominant source of π-delocalization and donor strength for the oxime moiety. O^{26} behaves differently: its p-rich lone pair (LP1) is oriented for σ-type hyperconjugation, donating into the C^{16}–C^{20} and C^{18}–C^{20} σ* orbitals (E(2) = 5.94 and 6.35 kcal/mol), whereas it is the more hybridized LP2 that donates into the aromatic ring π* system (C^{18}–C^{20} π*, E(2) = 4.37 kcal/mol). It is a comparatively weak interaction next to O^{30}'s. The two oxygens therefore do not share a single "p-rich lone pair drives resonance" rule: the identity of the resonance-active lone pair is swapped along with the hybridization pattern, with O^{30}'s p-rich LP2 acting as the stronger π-donor overall.

2.3.5. Natural Charges

NBO charges of the azo-oxime molecule (H_2L, **1**) were computed utilizing the B3LYP functional 6-311G(d,p) basis set. The computed charge distribution is listed in Table 5 and pictured in Figure S20. As listed in Table 5, atoms O^{26}, O^{30}, N^{11}, N^{12}, and N^{29} carry considerable negative charges of −0.69848, −0.50540, −0.20361, −0.21116, and −0.08894 a.u., correspondingly, with electronic configurations of [core]2s(1.68)2p(5.01), [core]2s(1.69)2p(4.81), [core]2s(1.39)2p(3.78), [core]2s(1.39)2p(3.79), and [core]2s(1.43)2p(3.63).

Table 5. The NOB charges of azo-oxime (H_2L, **1**) atoms by DFT/B3LYP//(6-311G(d,p).

Atom	NOB Charges	Atom	NOB Charges	Atom	NOB Charges
C22	−0.57547	C3	0.10627	H21	0.21448
C16	−0.22402	C13	0.11620	H9	0.21860
C1	−0.21108	C20	0.34916	H17	0.22309
C5	−0.20565	H32	0.15490	H31	0.42469
C14	−0.17796	H10	0.19898	H27	0.46778
C4	−0.17741	H25	0.20041	N12	−0.21116
C15	−0.17591	H23	0.20058	N11	−0.20361
C2	−0.17141	H7	0.20140	N29	−0.08894
C18	−0.11589	H24	0.20716	O26	−0.69848
C6	0.01510	H8	0.21046	O30	−0.50540
C28	0.02192	H19	0.21389		

These results indicate that these atoms serve as major electron-accepting centers and has a key role in facilitating intra-molecular charge transfer (ICT), with electron density flowing predominantly toward them rather than away. Overall, the NBO charges of the azo-oxime framework range from −0.69848 to 0.46778 a.u. The hydrogen atoms H^{27} and H^{31} exhibit the largest positive charges (0.46778 and 0.42469 a.u.), which can be attributed to their connection to greatly electronegatively oxygen atoms. Conversely, the heteroatoms O^{26} and O^{30}, along with C^{22}, possess the most negative charges, confirming their strong electron-withdrawing character and their contribution to charge delocalization within the molecule.

3. Optical Properties

Figure 4 shows the measured transmittance (T) and reflection (R) spectra for the azo-oxime ligand (H_2L) and its complex films. The films are found to be absorbing in the 355–580 nm spectral range while they are transparent for wavelengths larger than 580 nm. Within the absorbance range, there is an absorption edge due to the electron innervation from the supreme filled orbital to the minimal blank one. As shown in Figure 4, the film of azo-oxime ligand (H_2L film) has the greatest transmission; accordingly, it has the lowest reflection. So, the H_2L and it is complex films may be arranged according to

their transmission as **H_2L > VO^{2+}(2) > Cu^{2+}(3) > Cu^{2+}(4) > Cu^{2+}(5) > Fe^{3+}(6).** This implies that a lesser amount of light may pass through the film. As a result, the index of the film's refraction index generally increases, leading to the reduced of light as it goes through the film. The light fraction that is decelerated or twisted as it moves within the film is known as the film refraction. When a film has a greater refractive index, light moves through it more slowly than it would in a vacuum. Interactions with the atoms or molecules in the film enable light to move more slowly, lowering its velocity. Accordingly, a decrease in film transmittance signifies a decrease in the speed of light as it passes through the film and an increase in the refractive index (Figure 5). Where the n values have been estimated by using $R(\lambda)$ or $T(\lambda)$ values in the following relationships:

$$n(\lambda) = \frac{1 + R(\lambda)}{1 - R(\lambda)} \left(\frac{4R(\lambda)}{(1 - R(\lambda))^2} \right)^{0.5} \quad (30)$$

$$n(\lambda) = \frac{1}{T(\lambda)} \left(\frac{1}{(T(\lambda))^2} - 1 \right)^{0.5} \quad (31)$$

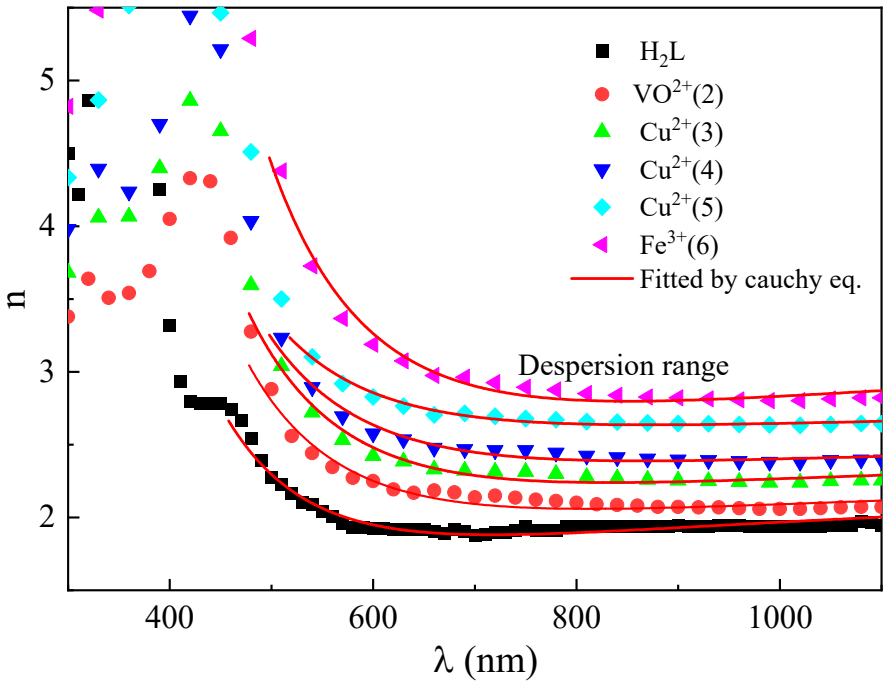

Figure 5. n versus λ for the film of azo-oxime and its complexes.

In addition, the film absorbance (A) was linked to the film transmittance (T) through this expression:

$$A(\lambda) = 2 - \log(T(\lambda)\%) \quad (32)$$

Hence, the film with the highest T values (H_2L film) has the smallest A values (Figures 4 and 6).

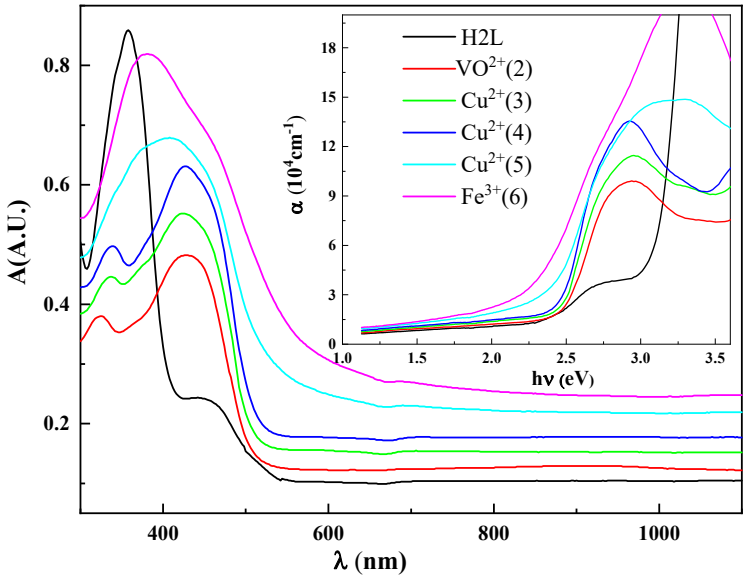

Figure 6. Absorbance spectrum and the inset shows α-λ dependence on the azo-oxime and its complex films.

However, the absorption edge of the H_2L film is in the 390–550 nm spectral range, while the absorption edges of various complex films were shifted at large wavelengths, i.e., redshift, as listed in Table 6. Fe^{3+}(**6**) film was shown to have a noteworthy impact. There are two noticeable ranges the spectra: Figure 7a shows the absorbance range where $T(\lambda) + R(\lambda) < 1.0$, where the extinction coefficient ($k(\lambda) = \alpha(\lambda)\lambda/(4\pi)$ and/or the absorption coefficient ($\alpha(\lambda)$) were related with the film absorption A through the formula $A(\lambda) = \alpha(\lambda).d$. The $\alpha(\lambda) - \lambda$ dependance azo-methine ligand (H_2L) and its complex films are shown in Figure 7b. The non-absorbing/transparent range where $T(\lambda) + R(\lambda) \approx 1.0$, the film becomes transparent and stops actively absorbing light. The optical properties of different films were inspected by means of Tauc's model, which helps to evaluate the value of the optical gap (E_g) using the α-hν dependence in the following form [86]:

$$\alpha h\nu = \beta^z (h\nu - E_g)^z \quad (33)$$

where β is the band-tail factor, z is Tauc's parameter which states the optical transitions kind ($z = 0.5$ and 2.0 for direct and indirect transitions, respectively) [87]. The optical transition mechanism and the precise evaluation of the indirect optical band gap (E_g) for the H_2L ligand and its metal complex films were systematically investigated using **Tauc's formulation** (Equation (33). To ensure high precision in the fitting procedure, the experimental absorption coefficient (α) was first computed across the absorption edge region. Subsequently, $\sqrt{\alpha h\nu}$ was plotted as a function of the incident photon energy ($h\nu$), as illustrated in Figure 7a. The fitting and evaluation procedure was executed via the following consecutive steps: **(1)** The fundamental absorption edge region where $\sqrt{\alpha h\nu}$ exhibits a strictly linear dependence on $h\nu$ was identified for each film sample. **(2)** A rigorous linear regression analysis (least-squares fitting method) was applied exclusively to this linear domain of the curve to determine the slope and intercept. **(3)** The resulting straight-line fit was mathematically extrapolated down to the photon energy axis where the absorption condition satisfies $\sqrt{\alpha h\nu} = 0$. The point of intersection on the horizontal $h\nu$-axis directly yields the value of the indirect optical band gap (E_g^{in}) as listed in Table 6. The excellent linearity observed in the absorption region ($R^2 > 0.99$) confirms that the indirect allowed transition model appropriately and accurately governs the optical absorption

process within these synthesized thin films. In the short absorption range α-hν dependance obeys the following expression:

$$\alpha = \alpha_o e^{h\nu/E_e} \quad (34)$$

where E_e is localized state width and α_o is constant. According to the above expression, $\ln(\alpha) - h\nu$ dependance are illustrated in Figure 7a where the E_e value was estimated as the reciprocal slope. The addition of some complexes, viz. VO^{2+}(**2**), Cu^{2+}(**3**), Cu^{2+}(**4**), Cu^{2+}(**5**), and Fe^{3+}(**6**) to the H_2L films, leads to rise in the E_e values (Table 6) which explains the observed decrease in E_g values as represented in Figure 7b. The obtained results are in excellent agreement with the Mott and Davis model, which states that the AC conductivity is inversely proportional to the optical band gap (E_g) value. The E_e values were correlated to β and n through E_e in the following relationship ($\beta = con$ ($\beta = 2.653 \times 10^{-3}\sigma_m/(n.E_e)$) where σ_m is the smallest metallic conductivity. The σ_m values have been boosted due to VO^{2+}(**2**), Cu^{2+}(**3**), Cu^{2+}(**4**), Cu^{2+}(**5**), and Fe^{3+}(**6**) complexes which are reliable to the observed decrease in E_g values.

Table 6. Optical parameters of azo-oxime and its complex films.

Compounds	H_2L	VO^{2+}(2)	Cu^{2+}(3)	Cu^{2+}(4)	Cu^{2+}(5)	Fe^{3+}(6)
Absorption edge range (nm)	360–410	440–480	460–500	440–510	450–520	460–540
E_g^{ind} (eV)	2.96	2.27	2.21	2.11	2.01	1.83
$\sqrt{A}$ ($\sqrt{\text{cm.eV}}$)	2279.03	1023.00	1079.97	967.00	864.94	663.93
σ_m (10^4 $\Omega^{-1}m^{-1}$)	21.87	5.10	6.60	6.05	6.15	21.87
λ_o (nm)	223.99	273.21	289.10	296.69	316.32	343.40
S_o (10^{14}) m^{-2}	8.10	5.93	6.40	6.54	6.89	8.11
E_o (eV)	5.55	4.55	4.30	4.19	3.93	3.62
E_d (eV)	22.55	20.15	23.01	24.13	27.10	34.62
n_o	2.25	2.33	2.52	2.60	2.81	3.25
ε_∞	5.06	5.43	6.35	6.76	7.90	10.56
ω_p (10^{15}) Hz	5.80	4.85	5.71	5.87	6.69	8.45
E_p (eV)	3.82	3.19	3.76	3.86	4.40	5.56
t_p (s)	1.72	2.06	1.75	1.70	1.49	1.18
N/m* (10^{53} kg^{-1} m^{-3})	7.37	5.15	7.12	7.53	9.79	164.82
N^{op} (10^{26} m^{-3})	2.69	1.88	2.60	2.74	3.57	60.06
μ^{op} ($C.s.kg^{-1}$)	7.57	9.06	7.70	7.49	6.57	5.20
ρ^{op} (Ω.m)	3.08	3.68	3.13	3.04	2.67	0.20
$X^{(3)}$ (10^{-12} esu)	1.095	1.547	3.294	4.425	9.092	33.613
n_2 (10^{-12} esu)	1.83	2.50	4.93	6.41	12.19	38.97

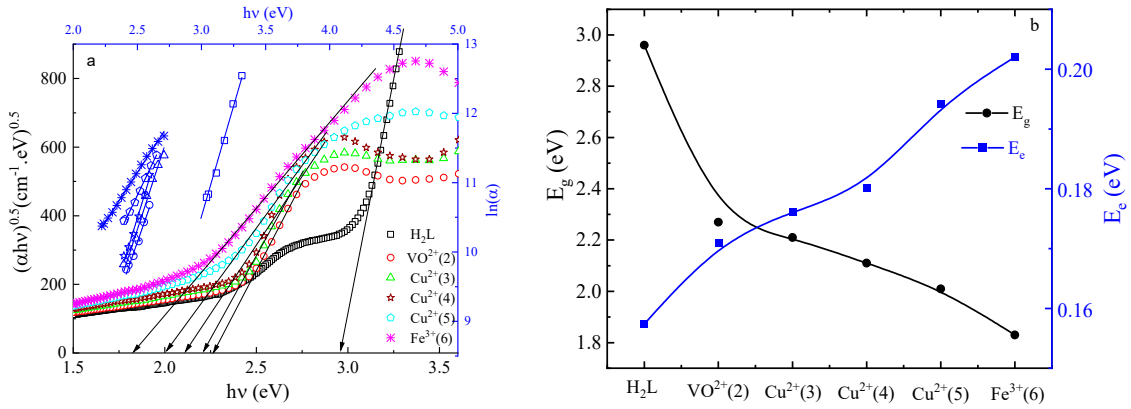

Figure 7. (**a**) The energy dependence of $(\alpha E)^{0.5}$ and $\ln(\alpha)$, (**b**) E_g and E_e values for the azo-oxime and its complex films.

4. Dispersion Parameters

In the high transparent area the refractive index n variation due to λ obeys Cauchy's dispersion relationship [88]:

$$n(\lambda) = a + b/\lambda^2 \quad (35)$$

where a and b, Cauchy's parameters which are given in Table 6, are the best fitting of the n values shown as a solid red line in Figure 6. Where λ tends to infinity, the second term of the above Equation (35) tends to zero. As a result, the static refractive index $n(0) = a$. Then Equation (35) takes the following form ($n(\lambda) = a$). Then the oscillator wavelength (λ_o) can be estimated with the help of the constant b ($b = n(0)\lambda_o^2$). The rise in λ_o values due to different complexes confirm the noted redshift in absorbance spectra as represented in Figure 7, i.e., decreases the values of E_g and the energy of single oscillator (E_o) ($E_o = 1240/\lambda_o$) [89]. The E_g value for the indirect transition scales the E_0 value ($E_0 \approx 2E_g$) [90] see Table 6). With the help of λ_o and $n(0)$ the oscillator strength (S_o) can be estimated as ($s_o = \left(n_0^2 - 1\right)/\lambda_o^2$). Then using S_o and E_o values the oscillator dispersion energy E_d can be estimated through the following expression $E_d = S_o(hc)^2/E_o$ [91]. The E_d values have been listed in Table 6 and found to rise due to different complexes. Such rise indicates a more polarized medium, which naturally slows down light, thus increasing the refractive index. An two important parameters, viz. the plasma frequency (ω_p) and the ratio of free carriers (N)/active electron mass (m*), can be estimated by using both E_g and $n(0)$ values in the following relationship [92]:

$$\omega_p = (n(0))^2 - 1)E_g^2/\hbar^2 \quad (36)$$

$$\frac{N}{m^*} = \frac{\varepsilon_0 (n(0))^2 - 1)^2 E_g^4}{4\pi\hbar^4 e^2}, \quad (37)$$

The values of ω_p and plasma energy ($E_p = \hbar\omega_p$) were found to increase alongside the dispersion energy for the complexes studied. This rise is primarily attributed to the increase in the N/m^* ratio, suggesting that the complexation process enhances the density of free charge carriers (N) or modifies the effective mass (m^*). Physically, the higher E_p reflects a stronger interaction between the electromagnetic field and the free electron gas within the complexes, which is consistent with the observed modulation in the refractive index and increased electronic polarizability of the samples. In other words, the simultaneous increase in E_d is associated with high polarity while the rise in E_p values is associated with free carrier density. This indicates that the prepared complexes have improved the linear and nonlinear optical properties of the material by enhancing the total electron density (bound and free). The semiconductor scattering time ($\boldsymbol{\tau}$) is the time undertaken by the charge to be defused and is known as the reciprocal of $\boldsymbol{\omega_P}$. A decrease in the value of τ occurs for the films with different metallic complexes. The semiconductor optical mobility (μ_{op}) is associated with the electronic bands' inherent dispersion, and it can be estimated with the help of m* values using the following relationship [93]:

$$\mu_{op} = e\tau/m^* \quad (38)$$

Then the optical resistance is given by [93]:

$$\rho_{op} = \left(e^2\tau\left(N_{op}/m^*\right)\right)^{-1} \quad (39)$$

All the calculated values are tabulated in Table 6. Both the μ_{op} and ρ_{op} values decrease with the increase in metal complexes. The related relationship between optical parameters

and metal complexes is shown in Figure 8. The observed changes in τ, μ_{op}, and ρ_{op} values are the same as observed for the optical band gap while the ω_P take the opposite behavior.

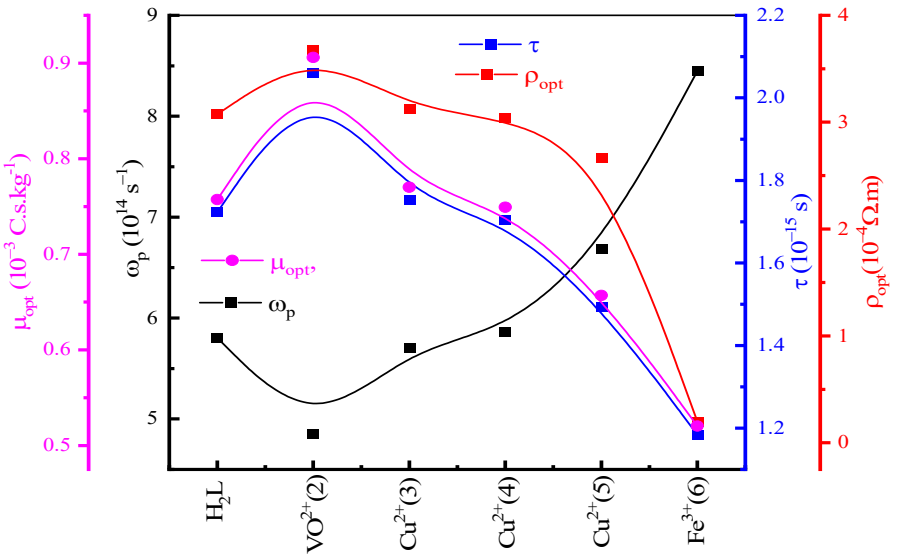

Figure 8. ω_p, τ_p, μ_{opt} and ρ_{opt} values for azo-oxime and its complex films.

As a metal complex is added to the azo-oxime films, the decrease in ρ_{op} values reflects a rise in optical conductivity which is consistent with the reduction in the energy gap, thereby facilitating electron transitions across the material. While the evaluation of practical device performance is required to confirm actual utility, these enhanced fundamental electronic and optical properties suggest that the films could serve as prospective baseline materials for future exploration in optoelectronic components, photoelectric devices, or flexible electronic research.

5. Nonlinear Optical Parameters

The prospective design of nonlinear optical systems, such as optical switches, modulators, and signal processing devices, fundamentally relies on a comprehensive understanding of the foundational nonlinear behavior of light-responsive materials [94]. The current study considers the nonlinear susceptibilities $X^{(1)}$ and $X^{(3)}$ and the nonlinear index of refraction (n_2) can be estimated by inserting the n values into the following expressions [20]:

$$X^{(1)} = \left(n^2 - 1\right)/4\pi \tag{40}$$

$$X^{(3)} = 1.7 \times 10^{-10}\left(\left(n^2 - 1\right)/(4\pi)\right)^4 \tag{41}$$

$$n_2 = 12\ \pi X^{(3)}/n \tag{42}$$

Table 6 lists the estimated values of $\chi^{(1)}$, $\chi^{(3)}$, and n_2 and shows their changes due to the complex additions to H_2L films. In optical thin films, the nonlinear refractive index (n_2) serves as an important parameter for understanding a material's fundamental response to high-intensity light, offering preliminary insights into its electronic polarizability. As shown in Table 6, (n_2) is closely related to the third-order nonlinear susceptibility ($\chi^{(3)}$) value. The variations in the estimated nonlinear optical constants between H_2L and its complex films can be attributed to structural differences induced by the metal centers. Although practical device architecture and operational performance were not evaluated in this study, examining these fundamental parameters provides foundational data regarding the films' nonlinear optical characteristics, indicating their theoretical interest for potential

future investigations in nonlinear optical fields. Parameters of the prepared azo-oxime complex films were compared with several recently reported metal complexes and related optical materials from the literature, as summarized in Table 7. As revealed in Table 7, the Fe^{3+} and Cu^{2+} complexes synthesized in this study exhibit exceptionally narrow optical band gaps (1.83–2.01 eV) and significantly enhanced third-order nonlinear susceptibilities ($\chi^{(3)}$) compared to several other oxime- and azo-based transition metal complexes. This noticeable enhancement in the nonlinear parameters indicates a highly polarizable electronic medium, thereby confirming the high significance and potential value of these films for future optimization in nonlinear optical applications. Measuring a film's optical conductivity (σ) is a useful method for examining its optical behavior and fully understanding how it responds to light. It is a broader concept that is significantly influenced by the electronic states present in the material, as opposed to electrical conductivity in the presence of alternating fields. The optical conductivity parts (real (σ_r) and imaginary (σ_i)) can be estimated with the help of n and k values using the following expressions [89]:

$$\sigma_1 = 0.17(2nk)\lambda^{-1}, \sigma_2 = 0.17\left(n^2 - k^2\right)\lambda^{-1} \quad (43)$$

Table 7. Comparison of optical and third-order nonlinear optical parameters of the synthesized films with related materials in the literature.

Material/Film	E_g^{ind}(eV)	$\chi^{(3)}$(10^{-12} esu)	n_2(10^{-12} esu)	Ref.
Fe^{3+}(**6**)	1.83	33.613	38.97	This work
Cu^{2+} (**5**)	2.01	9.092	12.19	This work
Cu^{2+} complex film of hydrazone oxime	2.11	2.5	5.37	[20]
Cu^{2+} complex film of hydrazone oxime	2.15	1.83	2.94	[19]
Transition metal complex film of Azo-Schiff base	1.95	12.14	15.3	[21]

Both of σ_1 and σ_2 were raised by raising hν or adding different complexes as shown in Figure 9. This raise in σ_1 and σ_2 is as a direct result of decreasing the E_g values, which is well discussed by Aly [95]. Apparently, that $\sigma_2 > \sigma_1$ values due to σ_2 is directly proportional to the real part of the dielectric constant ($\varepsilon_1 = n^2 - k^2$) while σ_1 is directly proportional to the imaginary part of the dielectric constant ($\varepsilon_2 = 2nk$). The E_g value of the Fe^{3+} complex film is the smallest value; therefore, it has the greatest σ_1 and σ_2 values. The energy dependence of ε_1 and ε_2 for azo-oxime ligand (H_2L) and its complex films is shown in Figure 10. As we see, the changes in ε_1 values due to energy are the same as the changes in n values. This is due to the real part of dielectric constant being linked to the dispersion of electromagnetic waves propagating in the film which advocates to reduce the speed of wave propagation within the film. On the other hand, the imaginary part of dielectric constant is responsible for the energy absorbed from the electric field due to the dipole moving. Accordingly, the rate of waves attenuated and/or disturbed within the film is specified by ε_2 [96,97]. Consequently, the E_g value is showed by the fitting line that crosses the x-axis.

The dielectric loss factor ($\tan(\delta) = \varepsilon_2/\varepsilon_1$) is the energy missing due to the phase-change at a certain frequency. Thermally produced relaxations, which are the only source of thermal energy removal and fully spinning dipoles, are the main cause of this loss. Ion hops that occur during electrical conduction at higher temperatures are the cause of this propensity [64]. The tan(δ) changes due to the photon energy are shown in Figure 11. The addition of different metal complexes leads to the rise in tan(δ) values. At shorter energies ($h\nu \leq 2.1$ eV) no significant changeover is seen. Conversely, when $h\nu > 2.1$ eV there is a rapid rise in tan(δ) values with the rise in $h\nu$. This indicates the onset of the absorption

edge (Figure 6) which was shifted to the shorter energies (redshift) due to the addition of different metal complexes. The Fe^{3+} film has a great shift occur. Such behavior of tan(δ) was previously noted for many films [20,98,99]. For amorphous materials, the density of states in the gap that limits the change in the tan(δ) values is denoted by the ε_1 values. A rise in the defect states in the complexes' films is indicated by such increasing tan(δ) values which also explain the observed decrease in the E_g values. An important parameter is the optical surface resistance (R_s) which is inversely proportional to the real part of conductivity ($R_s = \rho/t = 1/\sigma_1 t$). Another crucial parameter, namely thermal emissivity (ε_{th}), is affected by $h\nu$ or λ and it can be estimated with the help of R_s values as follows [100]:

$$\varepsilon_{th} = 1 - (1 + 2\varepsilon_o c R_s)^{-2} \quad (44)$$

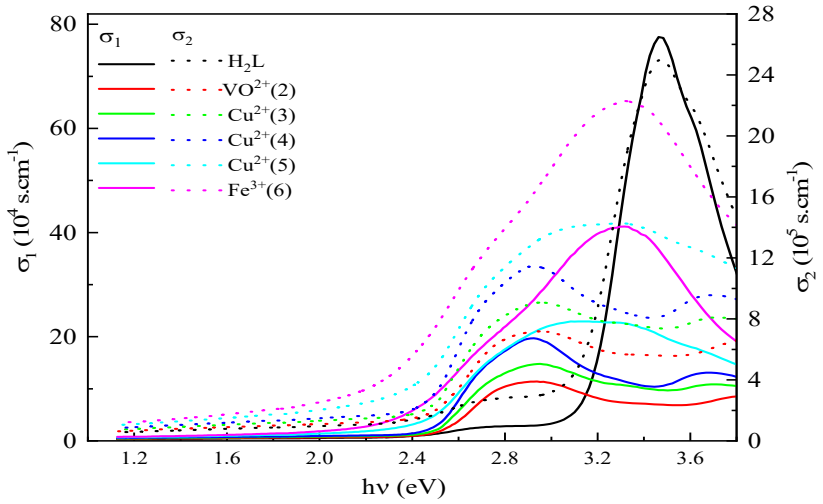

Figure 9. σ_1 and σ_2 vs. E for azo-oxime and its complex films.

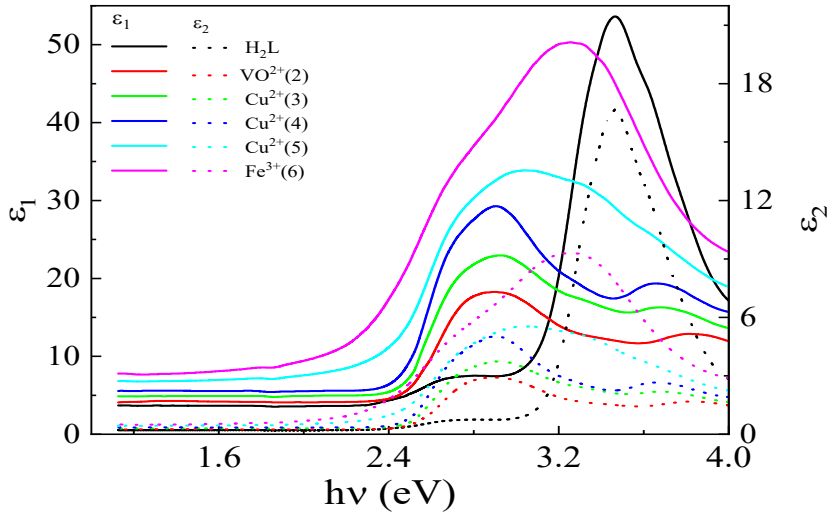

Figure 10. The energy dependence of ε_1 and ε_2 for azo-oxime and its complexes' films.

Both the R_s and ε_{th} values were plotted versus $h\nu$ for **H_2L** and its complex films (Figure 12). The change in R_s and ε_{th} due to $h\nu$ is opposing to the change in the optical conductivity (σ_r) which is consistent with the above Equation (44). For $h\nu$ less than the absorption edge begins (Table 6), both R_s and ε_{th} are approximately constant then quickly lowered to be constant again for $h\nu$ values larger than the absorption edge end. Moreover, the **H_2L** film has the greatest R_s and ε_{th} values. This is normally due to **H_2L** film having the largest value of E_g. The ε_{th} values are too small in comparison to the blackbody

(~1). Obviously, the ε_{th} value is affected by temperature, measurement direction, and other factors.

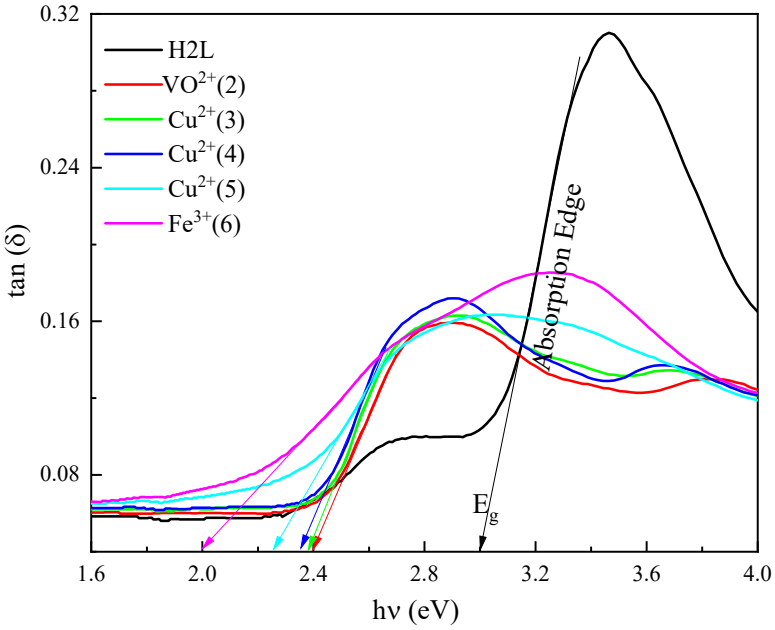

Figure 11. tan (δ) vs. hν for azo-oxime and its complexes' films.

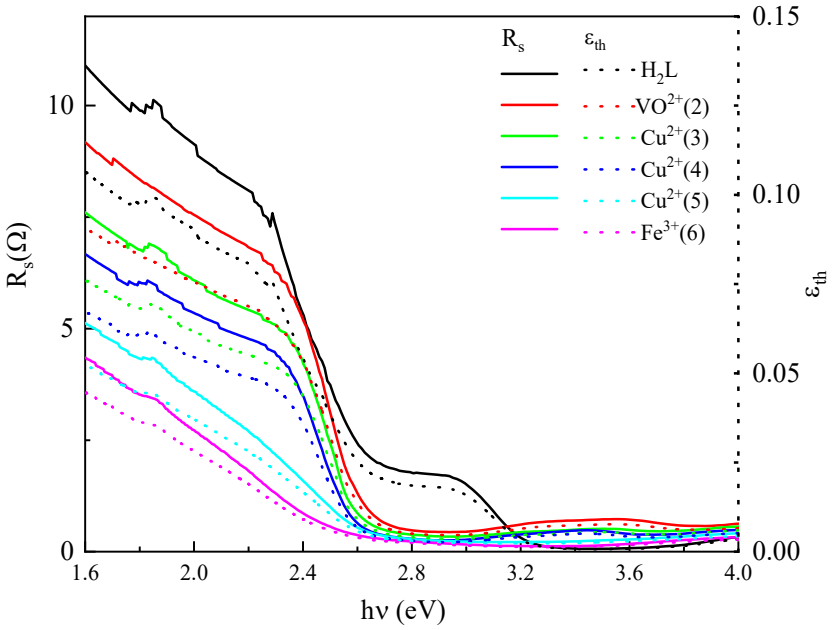

Figure 12. R_s vs. E and ε_{th} vs. E for azo-oxime and its complex films.

6. Influence of the Metal Ion on Structural, Electronic, and Optical Properties

Comparing VO^{2+}, Cu^{2+}, and Fe^{3+} complexes reveals a consistent, metal-dependent trend that links their structural, electronic, and optical behavior. Structurally, the d^1 VO^{2+} and d^9 Cu^{2+} complexes retain a distorted octahedral geometry arising from Jahn–Teller distortion (Cu^{2+}) or the asymmetric V=O bond (VO^{2+}), whereas complex (**5**) adopts a square-planar geometry, and the high-spin d^5 Fe^{3+} complex (**6**) shows the most pronounced octahedral distortion, consistent with its larger number of unpaired electrons (S = 5/2) and weaker ligand-field stabilization. Electronically, this structural progression is mirrored in the DFT-derived HOMO–LUMO gap (Table 4), which narrows steadily from the free ligand

(ΔE = 3.66 eV) to the VO^{2+} and Cu^{2+} complexes (ΔE = 3.15–3.60 eV) and drops sharply for the Fe^{3+} complex (ΔE = 2.01 eV), indicating that the Fe^{3+} center induces the greatest degree of electronic delocalization and reactivity, consistent with its higher global electrophilicity index (ω) and lower chemical hardness (η) relative to the other complexes (Table 4). This same trend is reproduced experimentally in the optical band gap of the thin films (Table 6): Eg decreases from 2.96 eV (H_2L) to 2.27, 2.21–2.01, and 1.83 eV for the VO^{2+}, Cu^{2+}, and Fe^{3+} complexes, respectively, closely paralleling the computed ΔE gap ordering. The agreement between the DFT-predicted electronic trend and the experimentally measured optical band gap trend across the series confirms that the identity of the coordinated metal ion through its d-electron configuration, ionic radius, and resulting coordination geometry is the primary factor governing the extent of electronic delocalization and optical response in these azo-oxime complexes, with Fe^{3+} producing the strongest narrowing effect, followed by Cu^{2+}, then VO^{2+}.

The computed HOMO-LUMO energy gap (ΔE, Table 4) and the experimentally determined optical band gap (e.g., from the α-hν analysis of the thin films, Table 6) are now compared directly across the series. Both quantities follow the same decreasing trend on going from the free ligand to the metal complexes: ΔE decreases from 3.66 eV (H_2L) to 3.60–3.15 eV (VO^{2+}/Cu^{2+} complexes) and 2.01 eV (Fe^{3+} complex), while the experimental Eg decreases correspondingly from 2.96 eV (H_2L) to 2.27–2.01 eV (VO^{2+}/Cu^{2+} complexes) and 1.83 eV (Fe^{3+} complex). Although the absolute values differ, as expected since DFT gas-phase HOMO–LUMO gaps and solid-state optical gaps derived from thin-film absorption edges are not numerically equivalent quantities, the two data sets track the same qualitative ordering (Fe^{3+} < Cu^{2+} < VO^{2+} < H_2L), and this agreement is now stated explicitly in the text rather than left for the reader to infer by comparing two separate tables. We further link this shared trend to the same underlying cause discussed in that subsection: increasing metal-induced electronic delocalization narrows both the calculated frontier-orbital gap and the measured optical absorption edge in parallel, which we use as mutual validation between the computational and experimental results.

To clearly establish the correlation between the investigated complexes and their prospective photo-related applications, it is essential to analyze how their fundamental physical constants meet the specific requirements of optoelectronic and photovoltaic technologies.

For photovoltaic and solar cell absorber applications, an ideal material must possess an optical band gap that matches the solar spectrum to maximize photon harvesting. The experimental results demonstrate that upon complexation, the optical band gap (E_g) narrows significantly from 2.96 eV for the free ligand down to 1.83 eV for the Fe^{3+} complex film. This strong redshift shifts the absorption edge deeper into the visible light region, which is highly favorable for effective solar energy conversion. Furthermore, this reduction in (E_g) closely correlates with the observed increase in the free charge carrier density-to-effective mass ratio ((N/m*), which enhances the material's optical conductivity (σ_1 and σ_2) under light illumination, thereby facilitating smoother electronic transitions across the transport gap.

For nonlinear optical (NLO) and switching applications, devices such as optical modulators and switches strictly rely on materials that exhibit strong light–matter interactions and fast electronic polarization under intense laser fields. The computational DFT and Molecular Electrostatic Potential (MEP) maps reveal that metal coordination induces substantial charge redistribution, leading to a dramatic rise in the dipole moments (up to 26.34 Debye). This highly asymmetric charge distribution creates a highly polarized electronic cloud. Experimentally, this structural polarization is verified by the exceptionally high values of third-order nonlinear optical susceptibility ($\boldsymbol{X}^{(3)}$) reaching 33.61 × 10^{-12} esu

for the Fe^{3+} film) and the nonlinear refractive index (n_2). Consequently, these findings provide a direct physical correlation showing that the strong electronic delocalization and high nonlinear parameters render these thin films promising candidates for future testing and optimization in optical signal processing and photonic switching layouts.

7. Measurements and Equipment

7.1. Materials

All the chemicals utilized are analytical grade and were employed without additional purifying. The cupric acetate dihydrate $Cu(CH_3COO)_2{\cdot}2H_2O$ (assay $\geq$ 99%), vanadyl sulphate trihydrate ($VOSO_4{\cdot}3H_2O$), cupric nitrate trihydrate $Cu(NO_3)_2{\cdot}3H_2O$ (assay $\geq$ 99.99%), cupric sulfate pentahydrate $CuSO_4{\cdot}5H_2O$ (assay $\geq$ 98%), and ferric chloride hexahydrate ($FeCl_3{\cdot}6H_2O$), *p*-Toluidine (99.6%), absolute ethanol (assay = 99.5%), HCl (37%), $NaNO_2$ (97%), 2-hydroxy benzaldehyde (99%), glacial acetic acid (assay = 99.7%), Hydroxylamine hydrochloride (assay = 99.0%) and DMSO (assay = 99.9%) were obtained from Merck (Merck KGaA, Darmstadt, Germany) or Sigma-Aldrich (Inc., St. Louis, MO, USA) Company. 2-hydroxy-5-(*p*-tolyldiazenyl)benzaldehyde was prepared by a previously reported method [101].

7.2. Physical Measurements and Analytical Techniques

At the Microanalytical Laboratory, Faculty of Science, Cairo University, Egypt, the contents of C, H, and N were examined. The complexes' metallic and chloride ion contents are identified by the earlier descripted methods [102,103]. The synthetics' IR spectrum (400–4000 cm^{-1}) was recorded by KBr plates on Perkin–Elmer-1430 (Perkin-Elmer, Waltham, MA, USA) (infrared spectrophotometer). The UV–Vis spectrum was measured in a 1 cm quartz cell (200–1100 nm) on a Shimadzu UV-Vis 1650-PC spectrophotometer (Shimadzu Corporation, Kyoto, Japan). On a JEOL ECA-400 spectrometer (JEOL Ltd., Tokyo, Japan), the ligand's NMR spectrum was recorded in DMSO-d6. On a Perkin Elmer 7 thermal analyzer (Perkin-Elmer, Waltham, MA, USA), the complexes' thermogravimetric analysis (TGA) was measured under a nitrogen (N_2) atmosphere (25 to 800 °C/HR 10 °C/min). A Gouy balance (Matthey's Balance)(Johnson Matthey, London, UK.) was used to measure the magnetic susceptibility at 298 K [104]. A Tacussel CD6NG conductivity bridge (Tacussel, Chelmsford, UK.) was used to test the complexes' molar conductance (10^{-3} M in DMSO at 25 °C), which was then computed using a standard formula [105]. On a Varian E-109 spectrophotometer (Varian Associates, Palo Alto, CA, USA) the solid complexes' Electron Spin Resonance (ESR) spectrum was recorded at room temperature using DPPH as a standard. Repeated attempts to get single crystals of the Cu^{2+}, VO^{2+}, and Fe^{3+} complexes suitable for single-crystal X-ray diffraction were unsuccessful. Using several mobile phases, thin-layer chromatography (TLC) was used to verify the synthetic chemicals' purity.

*7.3. Synthesis of the Ligand (H_2L, **1**)*

The azo-oxime, 2-hydroxy-5-(*p*-tolyldiazenyl) benzaldehyde oxime (H_2L, **1**) was synthesized by refluxing in the presence of sodium acetate a mixture of ethanolic solution of 2-hydroxy-5-(*p*-tolyldiazenyl)benzaldehyde (1 mmol, 240 mg) and hydroxylamine hydrochloride (1 mmol, 69.5 mg). After three hours, a colored solid that started to appear was removed and washed with hot ethanol, then dried over P_4O_{10} (Figure 13). Color: yellowish brown, m.p. 220 °C, (255 mg, 0.233 mmol, 91.3%). Elemental analysis (Anal.) for $C_{14}H_{13}N_3O_2$ (255.28 g /mol): Found (calc.) %C 65.45 (65.87), %H 4.89 (5.13), %N 16.09 (16.46). FT-IR (KBr, cm^{-1}), 3400 ν(OH), 3060w, 3023w, 2920w, 2850 ν(C-H), 1620 ν(C=N), 1480 ν(N=N), 1270 ν(C-O), 1010 ν(N-O). ^{1}H-NMR (DMSO-d_6, 300 MHz): δ(ppm) = 11.54,

(s, 1H, O*H*[27]), 11.06 (s, 1H, O*H*[31]), 8.40 (s, 1H, C*H*[32]), 8.11 (s, 1H, C-H[19]), 7.82 (s, 1H, CH[17]), 7.16 (d, 1H, CH[21]), 7.60 (d, 1H, CH[8&9]), 7.32 (d, 1H, CH[7&10]), 2.39 (s, 3H, CH[23–25]). ^{13}C-NMR (DMSO-d_6/90 Mhz): δ(ppm) = 150.50 (C3), 130.36 (C1&5), 122.82 (C2&4), 141.37 (C6), 146.10 (C13), 125.75 (C14), 121.76 (C15), 119.76 (C16), 1217.39 (C18), 159.24 (C20), 21.46 (C22), 145.46 (C28).

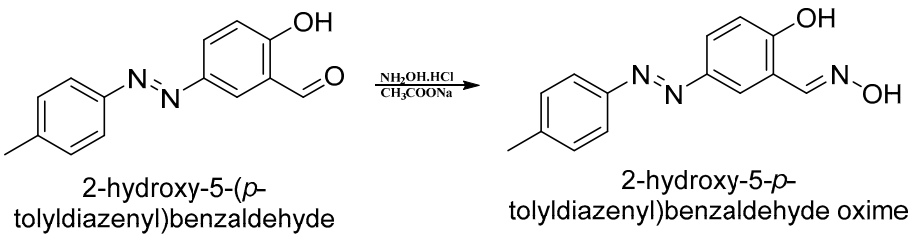

Figure 13. Synthesis of 2-hydroxy-5-(*p*-tolyldiazenyl)benzaldehyde oxime ligand (H_2L, **1**).

7.4. Procedure for Preparing the Complexes

The **Cu**$^{2+}$, **VO**$^{2+}$ and **Fe**$^{3+}$ complexes were prepared by refluxing an equimolar quantity of 2-hydroxy-5-(*p*-tolyldiazenyl) benzaldehyde oxime ligand (H_2L, **1**) (255 mg, 30 mL/EtOH) with the solution (EtOH/30 mL) of the following salts: $VOSO_4.3H_2O$ (217 mg), $Cu(CH_3COO)_2{\cdot}2H_2O$ (199.7 mg), $Cu(NO_3)_2.3H_2O$ (241.6 mg), and $CuSO_4{\cdot}5H_2O$ (249.7 mg) and $FeCl_3{\cdot}6H_2O$ (271.3 mg) in presence/absence of triethyl amine. After refluxing for 4 h, the resulting-colored precipitates were collected, washed with hot ethanol, and dried over P_4O_{10}.

7.4.1. VO^{2+}-Complex (**2**)

$[VO(H_2L)(SO_4)(H_2O)_2]$; Color: olive, yield (63.8%), m.p. > 300 °C, Λ_m = 21.3 ohm^{-1} cm^2 mol^{-1}. The elemental formula ($C_{14}H_{17}VN_3SO_9$, 454.30 g/mol): Found (calcd.) %C 36.68 (37.01), %H 3.87 (3.77), %N 9.00 (9.25), %VO 10.90 (11.21), %S 6.90 (7.06). FT-IR (KBr, cm^{-1}), 3445, 3200 ν(OH), 3060w, 3025, 2916w, 2873 ν(C-H), 1573 ν(C=N), 1480 ν(N=N), 1285 ν(C-OH), 1110 ν(N-OH), 963 ν(V=O), 580 ν(V←O), 473 ν(V←N).

7.4.2. Cu^{2+}-Complex (**3**)

$[Cu(H_2L)(OAc)_2(H_2O)_2]$; Color: olive, yield (63.8%), m.p. > 300 °C, Λ_m = 13.1 ohm^{-1} cm^2 mol^{-1}. The elemental formula $C_{18}H_{23}CuN_3O_8$, 472.94 g/mol): Found (calcd.) %C 45.49 (45.71), %H 4.87 (4.90), %N 9.61 (9.89), %Cu 13.00 (13.44). FT-IR (KBr, cm^{-1}), 3440, 3330 ν(OH), 3020w, 2930w, 2850 ν(C-H), 1595 ν(C=N), 1465 ν(N=N), 1305 ν(C-OH), 1050 ν(N-OH), 510 ν(Cu←O), 478 ν(Cu←N), 1540/1350(190) $\nu_s(CH_3COO)/\nu_{as}(CH_3COO)(\Delta)$.

7.4.3. Cu^{2+}-Complex (**4**)

$[Cu(H_2L)(NO_3)_2(H_2O)_2]$; Color: olive, yield (63.8%), m.p. > 300 °C, Λ_m = 17.3 ohm^{-1} cm^2 mol^{-1}. The elemental formula $C_{14}H_{17}CuN_5O_8$, 478.86 g/mol): Found (calcd.) %C 34.88 (35.12), %H 3.17 (3.58), %N 14.22 (14.63), %Cu 12.93 (13.27). FT-IR (KBr, cm^{-1}), 3545, 3330, 3440, 3350 ν(OH), 3022w, 2980w, 2930, 2850 ν(C-H), 1593 ν(C=N), 1475ν(N=N), 1308 ν(C-OH), 1077 ν(N-O), 512 ν(Cu←O), 479 ν(Cu←N), 1409, 1345, 920 ν (NO_3)(Δ = 64).

7.4.4. Cu^{2+}-Complex (**5**)

$[Cu(H_2L)(SO_4)(H_2O)]$; Color: olive, yield (63.8%), m.p. > 300 °C, Λ_m = 14.9 ohm^{-1}cm^{2}mol^{-1}. The elemental formula $C_{14}H_{15}CuN_3SO_7$, 432.89 g/mol): Found (calcd.) %C 38.55 (38.84), %H 3.09 (3.49), %N 9.44 (9.71), %Cu 14.77 (14.68), %S 6.99 (7.41). FT-IR (KBr, cm^{-1}), 3440, 3335 ν(OH), 3019w, 2990w, 2927 ν(C-H), 1590 ν(C=N), 1474 ν(N=N), 1290 ν(C-OH), 1055 ν(N-OH), 523 ν(Cu←O), 478 ν(Cu←N), 1190, 1055 ν(SO_4).

7.4.5. Fe^{3+}-Complex (**6**)

$[Fe(L)Cl_3(H_2O)].2H_2O$; Color: brown, yield (66.7%), m.p. > 300 °C, Λ_m = 24.1 $ohm^{-1}cm^2mol^{-1}$. The elemental formula ($C_{14}H_{19}FeN_3O_5Cl_3$, 471.52 g/mol): Found (calcd.) %C 35.31 (35.66), %H 3.79 (4.06), %N 8.91 (8.91), %Fe 11.58 (11.84), %Cl 22.11 (22.55). FT-IR (KBr, cm^{-1}), 3360, 3200 ν(OH), 3000w, 2960w, 2855 ν(C-H), 1575 ν(C=N), 1470 ν(N=N), 1301 ν(C-O), 1105 ν(N-O), 578 ν(Fe←O), 483 ν(Fe←N).

7.5. Density Functional Theory (DFT) Studies

To gain deeper insight into the molecular structure of the azo–oxime ligand and its Cu^{2+}, VO^{2+}, and Fe^{3+} complexes, geometry optimization and quantum chemical calculations were performed using Density Functional Theory (DFT) as implemented in the Gaussian 09 software package, with GaussView employed for visualization and analysis of the optimized geometries and associated molecular parameters. All calculations were carried out at the B3LYP hybrid exchange-correlation functional level, using the all-electron 6-311G(d, p) basis set for all atoms, including the Cu, V, and Fe metal centers, without the use of an effective core potential. Geometry optimizations were performed in the gas phase, with no symmetry constraints imposed on the starting geometries. Given the open-shell nature of the metal complexes, calculations were carried out using the unrestricted (UB3LYP) formalism, with spin multiplicities assigned consistent with the experimentally determined magnetic moments: a doublet ground state (S = 1/2, one unpaired electron) for the d^9 Cu^{2+} complexes and the d^1 VO^{2+} complex, and a high-spin sextet ground state (S = 5/2, five unpaired electrons) for the d^5 of Fe^{3+} complex, in agreement with the $^6A_{1g}$ term symbol derived from the electronic spectral analysis [68].

7.6. Preparation of Synthetic Films

Synthetic films were thermally deposited using a coating machine (Edward model E 306 A, Crawley, UK) onto cleaned quartz substrates under ambient temperature and vacuum pressure of ~2.5 10^{-4} Pa. The powder of H_2L and its complex metals were put in a Mo-boat that was gradually heated. The distance between the Mo-boat and substrates is 20 cm. The film thickness was ~200 nm, and the deposition rate (8 nm/s) was controlled by using a TM-350 MAXTEK, Inc., Cypress, CA, USA thickness monitor. For certainty, Tolansky's interferometric method was used to check the film thickness [106]. Both the film transmittance (T) and reflection (R) spectra were measured using a JASCO model V-570 UV-VIS-NIR spectrophotometer (JASCO Corporation, Tokyo, Japan) through the 300–1100 nm range.

8. Conclusions

Mononuclear complexes of Cu^{2+}, VO^{2+}, and Fe^{3+} with the oxime-based azo ligand 2-hydroxy-5-(p-tolyldiazenyl) benzaldehyde oxime (H_2L) were successfully synthesized via a straightforward equimolar reaction method. The obtained complexes were thoroughly characterized using elemental analysis, thermal techniques, and various spectroscopic tools, and the experimental findings were further supported by density functional theory (DFT) calculations. Spectral investigations revealed that azo oxime acts as a neutral bidentate chelating ligand, coordinating to the metal ions through the nitrogen atom of the protonated oxime group and the oxygen atom of the protonated phenolic hydroxyl group. The ESR spectra of Cu^{2+}, VO^{2+} complexes are typical to d^9 configuration with an axial symmetry type of a $d_{(x2-y2)}$ ground state and a significantly covalent environment. The metal centers adopt distorted octahedral geometries in all complexes. Computational studies performed at the DFT/B3LYP/6-311(pd) level provided valuable insight into the optimized geometries, dipole moments, frontier molecular orbitals (HOMO-LUMO), global

reactivity descriptors, and molecular electrostatic potential (MEP) maps. The theoretical results strongly supported the proposed structural features of the Cu^{2+}, VO^{2+}, and Fe^{3+} complexes. Moreover, the linear and nonlinear optical constants for H_2L and its complex films have been estimated and well discussed. Many different techniques are used to evaluate the optical bandgap value (E_g). The Fe^{3+} complex film has the smallest value of E_g value (1.83 eV), which is remarkably close to the E_g value of many semiconductors, viz. CdS_xSe_{1-x} alloys, Cu(In,Ga)Se, and CdSe. This renders the investigated films potential candidates for prospective exploration in various technological fields, such as solar cells, photo detectors, optical sensors, and infrared optics. Although the actual evaluation of device performance was not within the scope of this study, the obtained values indicate that the E_g value of H_2L and its VO^{2+}, Cu^{2+}(**3**), Cu^{2+}(**5**), and Fe^{3+}(**6**) complex films change between 2.96 and 1.83 eV, making them promising materials for further testing as an absorbance layer in solar cells, light-emitting diodes, photo detectors, and fiber optics. Based on n and k values, the complex dielectric constant and conductivity have been estimated. Also, the nonlinear refractive index (n_2), the first ($\chi^{(1)}$) and third ($\chi^{(3)}$) orders of nonlinear susceptibilities have been investigated. Based on these preliminary optical investigations, the ligand and its complex films exhibit encouraging fundamental constants that justify further research as potential future contenders for integration into signal processing, optical modulators, and switching designs, provided that practical device performance is thoroughly evaluated.

Supplementary Materials: The following supporting information can be downloaded at: https://www.mdpi.com/article/10.3390/inorganics14090244/s1.

Author Contributions: K.A.A.: Funding Acquisition, Methodology, Formal Analysis, Investigation, Supervisor, Project Administration, Resources. M.M.E.: Conceptualization, Data Curation, Formal Analysis, Funding Acquisition, Investigation, Methodology, Software, Supervision, Validation, Visualization, Writing—Original Draft Preparation, Writing—Review and Editing. T.M.S.: Formal Analysis, Funding Acquisition, Investigation, Methodology, Project Administration, Resources. All authors have read and agreed to the published version of the manuscript.

Funding: This work was funded by the University of Jeddah, Jeddah, Saudi Arabia, under grant No. (UJ-25-DR-20144). The authors, therefore, thank the University of Jeddah for technical and financial support.

Data Availability Statement: The original contributions presented in this study are included in the article/Supplementary Material. Further inquiries can be directed to the corresponding author.

Conflicts of Interest: The authors declare that they have no conflicts of interest.

References

1. Rahman, M.M.; Oni, A.O.; Gemechu, E.; Kumar, A. Assessment of energy storage technologies: A review. *En. Conv. Manag.* **2020**, *223*, 113295. [CrossRef]
2. Cheong, K.Y.; Impellizzeri, G.; Fraga, M.A. *Emerging Materials for Energy Conversion and Storage*; Elsevier: Amsterdam, The Netherlands, 2018.
3. Zhou, J.; Yu, X.; Zhou, J.; Lu, B. Polyimide/metal-organic framework hybrid for high performance Al–Organic battery. *Energy Storage Mater.* **2020**, *31*, 58–63. [CrossRef]
4. Ryoo, G.; Kim, S.K.; Lee, D.K.; Kim, Y.J.; Han, Y.S.; Jung, K.H. Energy Storage Performance of Electrode Materials Derived from Manganese Metal-Organic Frameworks. *Nanomaterials* **2024**, *14*, 503. [CrossRef] [PubMed]
5. Chettiannan, B.; Dhandapani, E.; Arumugam, G.; Rajendran, R.; Selvaraj, M. Metal-organic frameworks: A comprehensive review on common approaches to enhance the energy storage capacity in supercapacitor. *Coord. Chem. Rev.* **2024**, *518*, 216048. [CrossRef]
6. Sandhu, Z.A.; Raza, M.A.; Awwad, N.S.; Ibrahium, H.A.; Farwa, U.; Ashraf, S.; Dildar, A.; Fatima, E.; Ashraf, S.; Ali, F. Metal–organic frameworks for next-generation energy storage devices; a systematic review. *Mater. Adv.* **2024**, *5*, 30–50. [CrossRef]
7. Mirica, L.M.; Khusnutdinova, J.R. Structure and electronic properties of Pd(III) complexes. *Coord. Chem. Rev.* **2013**, *257*, 299–314. [CrossRef]

8. Xu, C.; Zhang, Z.-Y.; Ren, Z.-G.; Zhou, L.-K.; Li, H.-X.; Wang, H.-F.; Sun, Z.-R.; Lang, J.-P. Novel [Tp*WS_3Cu_2]-Based Coordination Compounds: Assembly, Crystal Structures, and Third-Order Nonlinear Optical Properties. *Cryst. Growth Des.* **2013**, *13*, 2530–2539. [CrossRef]
9. Irving, H.M.N.H. Coordination compounds in analytical chemistry. *Pure Appl. Chem.* **1978**, *50*, 1129–1146. [CrossRef]
10. Chen, C.-C.; Cai, Y.; Wang, L.-F.; Wu, Y.-D.; Yin, H.-J.; Zhou, J.-R.; Ni, C.-L.; Liu, W. Three Silver(I) Coordination Polymers Based on Pyridyl Ligands and Auxiliary Carboxylic Ligands: Luminescence and Efficient Sensing Properties. *Inorg. Chem.* **2021**, *60*, 5463–5473. [CrossRef] [PubMed]
11. Zhang, X.; Hu, J.; Li, J.; Liu, T.; Wang, J.; Ma, X. A bifunctional luminescent coordination polymer as recyclable sensor for detecting TNP and Fe^{3+} with high selectivity and sensitivity. *Inorg. Chim. Acta* **2019**, *486*, 556–561. [CrossRef]
12. Mingalev, P.G.; Olenin, A.Y.; Lisichkin, G.V. Partial Catalytic Oxidation of Alcohols: 2. Catalysts Based on Transition Metal Compounds (a Review). *Pet. Chem.* **2019**, *59*, 1–10. [CrossRef]
13. Ali, M.S.; El-Saied, F.A.; Shakdofa, M.M.E.; Karnik, S.; Jaragh-Alhadad, L.A. Synthesis and characterization of thiosemicarbazone metal complexes: Crystal structure, and antiproliferation activity against breast (MCF7) and lung (A549) cancers. *J. Mol. Struct.* **2023**, *1274*, 134485. [CrossRef]
14. Medici, S.; Peana, M.; Crisponi, G.; Nurchi, V.M.; Lachowicz, J.I.; Remelli, M.; Zoroddu, M.A. Silver coordination compounds: A new horizon in medicine. *Coord. Chem. Rev.* **2016**, *327–328*, 349–359. [CrossRef]
15. Malinowski, J.; Zych, D.; Jacewicz, D.; Gawdzik, B.; Drzeżdżon, J. Application of Coordination Compounds with Transition Metal Ions in the Chemical Industry—A Review. *Int. J. Mol. Sci.* **2020**, *21*, 5443. [CrossRef] [PubMed]
16. Wang, Y.; Tian, J.; Sun, Z.; Wang, L.; Xu, R.; Li, M.; Chen, Z. A comprehensive review of battery modeling and state estimation approaches for advanced battery management systems. *Renew. Sustain. Energy Rev.* **2020**, *131*, 110015. [CrossRef]
17. Liu, S.; Wei, L.; Wang, H. Review on reliability of supercapacitors in energy storage applications. *Appl. Energy* **2020**, *278*, 115436. [CrossRef]
18. Shakdofa, M.M.E.; El-Saied, F.A.; Rasras, A.J.; Al-Hakimi, A.N. Transition metal complexes of a hydrazone–oxime ligand containing the isonicotinoyl moiety: Synthesis, characterization and microbicide activities. *Appl. Organomet. Chem.* **2018**, *32*, e4376. [CrossRef]
19. Morsy, N.A.; Aly, K.A.; Mohery, M.; Ebrahium, M.M.; Kumar, E.R. Optical characteristics of synthetic Cu^{2+} complex films derived from 4-chloro-N-(3-(hydroxyimino) butan-2-ylidene) benzohydrazide for optoelectronic and photovoltaic applications. *J. Mol. Struct.* **2024**, *1316*, 138820. [CrossRef]
20. Saleem, Q.M.; Ebrahium, M.M.; Aly, K.A.; Saddeek, Y.B. Optical properties of transition metals complex films derived from hydrazone oxime for optoelectronic devices. *J. Mol. Struct.* **2025**, *1321*, 140196. [CrossRef]
21. Shatir, T.M.; Aly, K.A.; Ebrahium, M.M.; Saddeek, Y.B.; Ranjith Kumar, E. Linear and non-linear optical and dielectric properties of transition metals complexes films derived from Azo-Schiff base for photovoltaic applications. *J. Mol. Liq.* **2024**, *401*, 124636. [CrossRef]
22. Zhang, Q.; Liu, Z.; Zhao, B.; Cheng, Y.; Zhang, L.; Wu, H.-H.; Wang, M.-S.; Dai, S.; Zhang, K.; Ding, D.; et al. Design and understanding of dendritic mixed-metal hydroxide nanosheets@N-doped carbon nanotube array electrode for high-performance asymmetric supercapacitors. *Energy Storage Mater.* **2019**, *16*, 632–645. [CrossRef]
23. Geary, W.J. The use of conductivity measurements in organic solvents for the characterisation of coordination compounds. *Coord. Chem. Rev.* **1971**, *7*, 81–122. [CrossRef]
24. Serbest, K.; Dural, T.; Emirik, M.; Zengin, A.; Faiz, Ö. Heteroligand bivalent transition metal complexes with an azo-oxime ligand and 1,10-phenanthroline: Synthesis, spectroscopy, thermal analysis, DFT calculations and SOD-mimetic activities. *J. Mol. Struct.* **2021**, *1229*, 129579. [CrossRef]
25. Korkmaz, Ü.; Findik, B.T.; Dede, B.; Karipcin, F. Synthesis, structural elucidation, in vitro antibacterial activity, DFT calculations, and molecular docking aspects of mixed-ligand complexes of a novel oxime and phenylalanine. *Bioorg. Chem.* **2022**, *121*, 105685. [CrossRef] [PubMed]
26. Chitrapriya, N.; Mahalingam, V.; Zeller, M.; Lee, H.; Natarajan, K. Synthesis, characterization, DNA binding and cleavage studies of Ru(II) complexes containing oxime ligands. *J. Mol. Struct.* **2010**, *984*, 30–38. [CrossRef]
27. El-Aarag, B.; El-Saied, F.; Salem, T.; Khedr, N.; Khalifa, S.A.M.; El-Seedi, H.R. New metal complexes derived from diacetylmonoxime-n(4)antipyrinylthiosemicarbazone: Synthesis, characterization and evaluation of antitumor activity against Ehrlich solid tumors induced in mice. *Arab. J. Chem.* **2021**, *14*, 102993. [CrossRef]
28. Aslan, H.G.; Özcan, S.; Karacan, N. Synthesis, characterization and antimicrobial activity of salicylaldehyde benzenesulfonylhydrazone (Hsalbsmh)and its Nickel(II), Palladium(II), Platinum(II), Copper(II), Cobalt(II) complexes. *Inorg. Chem. Commun.* **2011**, *14*, 1550–1553. [CrossRef]
29. El-Wahab, Z.H.A.; Mashaly, M.M.; Salman, A.A.; El-Shetary, B.A.; Faheim, A.A. Co(II), Ce(III) and UO_2(VI) bis-salicylatothiosemicarbazide complexes: Binary and ternary complexes, thermal studies and antimicrobial activity. *Spectrochim. Acta Part A Mol. Biomol. Spectrosc.* **2004**, *60*, 2861–2873. [CrossRef] [PubMed]

30. Pavia, D.L.; Lampman, G.M.; Kriz, G.S.; Vyvyan, J.R. *Introduction to Spectroscopy*, 5th ed.; Cengage Learning: Independence, KY, USA, 2013.
31. Shakdofa, M.M.E.; Morsy, N.A.; Rasras, A.J.; Al-Hakimi, A.N.; Shakdofa, A.M.E. Synthesis, characterization, and density functional theory studies of hydrazone–oxime ligand derived from 2,4,6-trichlorophenyl hydrazine and its metal complexes searching for new antimicrobial drugs. *Appl. Organomet. Chem.* **2021**, *35*, e6111. [CrossRef]
32. Nakamoto, K. *Infrared and Raman Spectra of Inorganic and Coordination Compounds Part B: Applications in Coordination, Organometallic, and Bioinorganic Chemistry*, 6th ed.; John Wiley & Sons INC: Hoboken, NJ, USA, 2009; p. 424.
33. Saleem, Q.M.; Ebrahium, M.M.; Al-Hakimi, A.N.; Shakdofa, A.M. Ligational behavior of bidentate NO-donor, 2-(((1H-1,2,4-triazol-5-yl)imino)methyl)-4-(o-tolyldiazenyl)phenol towards VO^{2+}, Fe^{3+}, Ru^{3+}, Co^{2+}, Mn^{2+}, Ni^{2+}, Cu^{2+} Zn^{2+} and ions preparation, experimental, theoretical characterization, and microbicidal investigation. *J. Taibah Univ. Sci.* **2024**, *18*, 2289692. [CrossRef]
34. Pandhurnekar, C.P.; Meshram, E.M.; Chopde, H.N.; Batra, R.J. Synthesis, Characterization, and Biological Activity of 4-(2-Hydroxy-5-(aryl-diazenyl)phenyl)-6-(aryl)pyrimidin-2-ols Derivatives. *Org. Chem. Inter.* **2013**, *2013*, 582079. [CrossRef]
35. Baeva, L.A.; Biktasheva, L.F.; Fatykhov, A.A.; Lyapina, N.K. Condensation of acetylacetone with formaldehyde and thiols. *Russ. J. Org. Chem.* **2013**, *49*, 1283–1286. [CrossRef]
36. Rageh, N.M.; Mawgoud, A.M.A.; Mostafa, H.M. Electronic spectra, solvatochromic behaviour, and acidity constants of some new azocoumarin derivatives. *Chem. Pap.* **1999**, *53*, 107–113.
37. Gup, R.; Kirkan, B. Synthesis and spectroscopic studies of copper(II) and nickel(II) complexes containing hydrazonic ligands and heterocyclic coligand. *Spectrochim. Acta–Part A Mol. Biomol. Spectrosc.* **2005**, *62*, 1188–1195. [CrossRef] [PubMed]
38. Reddy, S.L.; Endo, T.; Reddy, G.S. *Electronic (Absorption) Spectra of 3d Transition Metal Complexes, Advanced Aspects of Spectroscopy*; InTech: Rijeka, UK, 2012.
39. Lever, A.B.P. *Inorganic Electronic Spectroscopy*; Elsevier Science: Amsterdam, The Netherlands, 1984; p. 863.
40. Sreeja, P.B.; Kurup, M.R.P. Synthesis and spectral characterization of ternary complexes of oxovanadium(IV) containing some acid hydrazones and 2,2′-bipyridine. *Spectrochim. Acta Part A Mol. Biomol. Spectrosc.* **2005**, *61*, 331–336. [CrossRef] [PubMed]
41. Sathyanarayana, D.N. *Electronic Absorption Spectroscopy and Related Techniques*; Universities Press: Hyderabad, India, 2001; p. 526.
42. El-Saied, F.A.; Shakdofa, M.M.E.; El-Tabl, A.S.; Abd-Elzaher, M.M.A. Coordination behaviour of N'^{1},N'^{4}-bis((1, 5-dimethyl-3-oxo-2-phenyl-2,3-dihydro-1H-pyrazol-4-yl)methylene) succinohydrazide toward transition metal ions and their antimicrobial activities. *Main Group Chem.* **2014**, *13*, 87–103. [CrossRef]
43. Hanson, G.R.; Kabanos, T.A.; Keramidas, A.D.; Mentzafos, D.; Terzis, A. Oxovanadium(IV)-amide binding. Synthetic, structural, and physical studies of {N-[2-(4-oxopent-2-en-2-ylamino)phenyl]pyridine-2-carboxamido}oxovanadium(IV) and {N-[2-(4-phenyl-4-oxobut-2-en-2-ylamino)phenyl]pyridine-2-carboxamido}oxo- vanadium(IV). *Inorg. Chem.* **1992**, *31*, 2587–2594. [CrossRef]
44. El-Tabl, A.S.; Shakdofa, M.M.E.; Shakdofa, A.M.E. Metal complexes of N′-[2-hydroxy-5-(phenyldiazenyl)-benzylidene] isonicotinohydrazide. Synthesis, spectroscopic characterization and antimicrobial activity. *J. Serb. Chem. Soc.* **2013**, *78*, 39–55. [CrossRef]
45. Dong, Y.; Narla, R.K.; Sudbeck, E.; Uckun, F.M. Synthesis, X-ray structure, and anti-leukemic activity of oxovanadium(IV) complexes. *J. Inorg. Biochem.* **2000**, *78*, 321–330. [CrossRef] [PubMed]
46. Dodwad, S.S.; Dhamnaskar, R.S.; Prabhu, P.S. Electron spin resonance spectral studies of vanadyl complexes with some schiff bases. *Polyhedron* **1989**, *8*, 1748–1750. [CrossRef]
47. Raman, N.; Pitchaikani Raja, Y.; Kulandaisamy, A. Synthesis and characterisation of Cu(II), Ni(II), Mn(II), Zn(II) and VO(II) Schiff base complexes derived from o-phenylenediamine and acetoacetanilide. *Proc. Indian Acad. Sci. (Chem. Sci.)* **2001**, *113*, 183–189. [CrossRef]
48. Patron, M.; Kivelson, D.; Schwartz, R.N. Electron spin resonance spectra of vanadyl acetylacetonate in n-alkanes. A study of rotational relaxation. *J. Phys. Chem.* **1982**, *86*, 518–524. [CrossRef]
49. Walker, F.A.; Carlin, R.L.; Rieger, P.H. ESR Studies of Coordination to the Sixth Position of Vanadyl Acetylacetonate. *J. Chem. Phys.* **1966**, *45*, 4181–4189. [CrossRef]
50. McGarvey, B.R.; Tepper, E.L. Paramagnetic resonance absorption studies in the autoxidation of titanium(III) and vanadium(III) trisacetylacetonates. *Inorg. Chem.* **1969**, *8*, 498–505. [CrossRef]
51. Zaky, R.R.; Ibrahim, K.M.; Gabr, I.M. Bivalent transition metal complexes of o-hydroxyacetophenone [N-(3-hydroxy-2-naphthoyl)] hydrazone: Spectroscopic, antibacterial, antifungal activity and thermogravimetric studies. *Spectrochim. Acta Part A Mol. Biomol. Spectrosc.* **2011**, *81*, 28–34. [CrossRef] [PubMed]
52. Hathaway, B.J.; Billing, D.E. The electronic properties and stereochemistry of mono-nuclear complexes of the copper(II) ion. *Coord. Chem. Rev.* **1970**, *5*, 143–207. [CrossRef]
53. Brown, D.R.; West, D.X. An ESR study of addition species formed between bis(2-thiopyridine N-oxide)Cu(II) and heterocyclic and aliphatic amines. *J. Inorg. Nucl. Chem.* **1981**, *43*, 1017–1021. [CrossRef]

54. Nagashri, K.; Joseph, J.; Dhanaraj, C.J. Copper(II) complexes of hydroxyflavone derivatives as potential bioactive molecule to combat antioxidants: Synthesis, characterization and pharmacological activities. *Appl. Organomet. Chem.* **2011**, *25*, 704–717. [CrossRef]
55. Tomlinson, A.A.G.; Hathaway, B.J. The electronic properties and stereochemistry of the copper(II) ion. Part II. The monoamine adducts of bisethylenediaminecopper(II) complexes. *J. Chem. Soc. A Inorg. Phys. Theo.* **1968**, *3*, 1685–1688. [CrossRef]
56. El-Tabl, A.S.; Aly, F.A.; Shakdofa, M.M.E.; Shakdofa, A.M.E. Synthesis, characterization, and biological activity of metal complexes of azohydrazone ligand. *J. Coord. Chem.* **2010**, *63*, 700–712. [CrossRef]
57. Al-Hakimi, A.N.; El-Tabl, A.S.; Shakdofa, M.M.E. Coordination and biological behaviour of 2-(p-toluidino)-N′-(3-oxo-1,3-diphenylpropylidene) acetohydrazide and its metal complexes. *J. Chem. Res.* **2009**, *2009*, 770–774. [CrossRef]
58. El-Tabl, A.S.; Shakdofa, M.M.E.; Whaba, M.A. Synthesis, characterization and fungicidal activity of binary and ternary metal(II) complexes derived from 4,4′-((4-nitro-1,2-phenylene) bis(azanylylidene))bis(3-(hydroxyimino)pentan-2-one). *Spectrochim. Acta Part A Mol. Biomol. Spectrosc.* **2015**, *136*, 1941–1949. [CrossRef] [PubMed]
59. Kivelson, D.; Neiman, R. ESR Studies on the Bonding in Copper Complexes. *J. Chem. Phys.* **1961**, *35*, 149–155. [CrossRef]
60. Mangalam, N.A.; Prathapachandra Kurup, M.R. Versatile binding properties of a di-2-pyridyl ketone nicotinoylhydrazone ligand: Crystal structure of a Cu(II) complex. *Spectrochim. Acta Part A Mol. Biomol. Spectrosc.* **2011**, *78*, 926–934. [CrossRef] [PubMed]
61. Shauib, N.M.; Elassar, A.Z.A.; El-Dissouky, A. Synthesis and spectroscopic characterization of copper(II) complexes with the polydentate chelating ligand 4,4′-[1,4-phenylenedi(nitrilo)dipente-2-one. *Spectrochim. Acta Part A Mol. Biomol. Spectrosc.* **2006**, *63*, 714–722. [CrossRef] [PubMed]
62. Ray, R.K.; Kauffmann, G.B. An EPR study of copper(II)-substituted biguanide complexes. Part III. *Inorg. Chim. Acta* **1990**, *174*, 237–244. [CrossRef]
63. Ray, R.K.; Kauffman, G.B. An EPR study of some copper(II) coordination compounds of substituted biguanides. Part IV. *Inorg. Chim. Acta* **1990**, *174*, 257–262. [CrossRef]
64. El-Tabl, A.S. Synthesis and spectral studies on mononuclear copper(II) complexes of isonitrosoacetylacetone ligand. *Pol. J. Chem.* **1997**, *71*, 1213–1222.
65. Swamy, B.; Swamy, J.R. Preparation and characterization of some transition metal complexes of benzoic acid hydrazones of 2-aminonicotinaldehyde. *Transit. Met. Chem.* **1991**, *16*, 35–38. [CrossRef]
66. Yang, L.; Powell, D.R.; Houser, R.P. Structural variation in copper(i) complexes with pyridylmethylamide ligands: Structural analysis with a new four-coordinate geometry index, τ4. *Dalton Trans.* **2007**, 955–964. [CrossRef] [PubMed]
67. Ismael, M.; Abdou, A.; Abdel-Mawgoud, A.-M. Synthesis, Characterization, Modeling, and Antimicrobial Activity of FeIII, CoII, NiII, CuII, and ZnII Complexes Based on Tri-substituted Imidazole Ligand. *Z. Anorg. Allg. Chem.* **2018**, *644*, 1203–1214. [CrossRef]
68. Frisch, M.J.; Trucks, G.W.; Schlegel, H.B.; Scuseria, G.E.; Robb, M.A.; Cheeseman, J.R.; Scalmani, G.; Barone, V.; Petersson, G.A.; Nakatsuji, H.; et al. *Gaussian 09, Revision A02*; Gaussian, Inc: Wallingford CT, USA, 2016.
69. Waheeb, A.S.; Awad, M.A.; Kyhoiesh, H.A.K.; Kadhum, A.M.; Thabit, J.A.; Lazam, S.A. Synthesis, and characterization of Ni(II), and Cu(II) metal complexes containing new azo dye ligand (N,N,N) and evaluation of their biological activities supported by DFT studies, molecular docking, ADMET profiling, drug-likeness analysis and toxicity prediction. *J. Mol. Struct.* **2025**, *1321*, 139867. [CrossRef]
70. Güleryüz, C.; Hasan, D.M.; Awad, M.A.; Waheeb, A.S.; Hassan, A.U.; Mohyuddin, A.; Kyhoiesh, H.A.K.; Alotaibi, M.T. Molecular engineering on tyrian puprle natural dye as TiO2 based fined tuned photovoltaic dye material: DFT molecular analysis. *J. Mol. Graph. Model.* **2025**, *134*, 108894. [CrossRef] [PubMed]
71. Parr, R.G.; Szentpály, L.v.; Liu, S. Electrophilicity Index. *J. Am. Chem. Soc.* **1999**, *121*, 1922–1924. [CrossRef]
72. Wang, L.; Ding, J.; Pan, L.; Cao, D.; Jiang, H.; Ding, X. Quantum chemical descriptors in quantitative structure–activity relationship models and their applications. *Chemom. Intell. Lab. Syst.* **2021**, *217*, 104384. [CrossRef]
73. Gázquez, J.L.; Cedillo, A.; Vela, A. Electrodonating and Electroaccepting Powers. *J. Phys. Chem. A* **2007**, *111*, 1966–1970. [CrossRef] [PubMed]
74. Chattaraj, P.K.; Chakraborty, A.; Giri, S. Net Electrophilicity. *J. Phys. Chem. A* **2009**, *113*, 10068–10074. [CrossRef] [PubMed]
75. Domingo, L.R.; Chamorro, E.; Pérez, P. Understanding the Reactivity of Captodative Ethylenes in Polar Cycloaddition Reactions. A Theoretical Study. *J. Org. Chem.* **2008**, *73*, 4615–4624. [CrossRef] [PubMed]
76. Kiyooka, S.-i.; Kaneno, D.; Fujiyama, R. Intrinsic reactivity index as a single scale directed toward both electrophilicity and nucleophilicity using frontier molecular orbitals. *Tetrahedron* **2013**, *69*, 4247–4258. [CrossRef]
77. Ayers, P.W.; Anderson, J.S.M.; Rodriguez, J.I.; Jawed, Z. Indices for predicting the quality of leaving groups. *Phys. Chem. Chem. Phys.* **2005**, *7*, 1918–1925. [CrossRef] [PubMed]
78. Politzer, P.; Murray, J.S. The fundamental nature and role of the electrostatic potential in atoms and molecules. *Theor. Chem. Acc.* **2002**, *108*, 134–142. [CrossRef]

79. Eşme, A.; Sağdınç, S.G. Spectroscopic (FT–IR, FT–Raman, UV–Vis) analysis, conformational, HOMO-LUMO, NBO and NLO calculations on monomeric and dimeric structures of 4–pyridazinecarboxylic acid by HF and DFT methods. *J. Mol. Struct.* **2017**, *1147*, 322–334. [CrossRef]
80. Politzer, P.; Truhlar, D.G. *Chemical Applications of Atomic and Molecular Electrostatic Potentials: Reactivity, Structure, Scattering, and Energetics of Organic, Inorganic, and Biological Systems*, 1st ed.; Springer: New York, NY, USA, 1981. [CrossRef]
81. Snehalatha, M.; Ravikumar, C.; Hubert Joe, I.; Sekar, N.; Jayakumar, V.S. Spectroscopic analysis and DFT calculations of a food additive Carmoisine. *Spectrochim. Acta Part A Mol. Biomol. Spectrosc.* **2009**, *72*, 654–662. [CrossRef] [PubMed]
82. Wojciechowski, P.; Płoszaj, P. Structural, vibrational, NBO and quantum chemical analysis of two novel antimycobacterial compounds. *J. Mol. Struct.* **2020**, *1218*, 128409. [CrossRef]
83. Glendening, E.D.; Landis, C.R.; Weinhold, F. NBO 6.0: Natural bond orbital analysis program. *J. Comput. Chem.* **2013**, *34*, 1429–1437. [CrossRef] [PubMed]
84. Kaur, M.; Sheena Mary, Y.; Varghese, H.T.; Yohannan Panicker, C.; Yathirajan, H.S.; Siddegowda, M.S.; Alsenoy, C.V. Vibrational spectroscopic, molecular structure, first hyperpolarizability and NBO studies of 4′-methylbiphenyl-2-carbonitrile. *Spectrochim. Acta Part A Mol. Biomol. Spectrosc.* **2012**, *98*, 91–99. [CrossRef] [PubMed]
85. Glendening, E.; Reed, A.; Carpenter, J.; Weinhold, F. *Nbo Version 3.1, Tci*; University of Wisconsin: Madison, WI, USA, 1998; Volume 65.
86. Tauc, J.; Grigorovici, R.; Vancu, A. Optical Properties and Electronic Structure of Amorphous Germanium. *Phys. Status Solidi (B)* **1966**, *15*, 627–637. [CrossRef]
87. Aly, K.A.; Dahshan, A.; Saddeek, Y. Optical properties of as-prepared and irradiated In–Cd–Se thin films. *J. Mater. Sci. Mater. Electron.* **2022**, *33*, 12663–12673. [CrossRef]
88. DrDomenico, M., Jr.; Wemple, S.H. Oxygen-Octahedra Ferroelectrics. I. Theory of Electro-optical and Nonlinear optical Effects. *J. Appl. Phys.* **2003**, *40*, 720–734. [CrossRef]
89. Aly, K.A. Comment on the relationship between electrical and optical conductivity used in several recent papers published in the journal of materials science: Materials in electronics. *J. Mater. Sci. Mater. Electron.* **2022**, *33*, 2889–2898. [CrossRef]
90. Aly, K.A. On the study of the optical constants for different compositions of $Sn_x(GeSe)_{100-x}$ thin films in terms of the electronic polarizability, electronegativity and bulk modulus. *Appl. Phys. A Mater. Sci. Process.* **2015**, *120*, 293–299. [CrossRef]
91. Sharda, S.; Sharma, E.; Aly, K.A.; Dahshan, A.; Sharma, P. High refractive index (Dy) doped $(GeTe_2)_{80}(In_2Te_3)_{20}$ thin films for sub-THz and millimeter-wave applications. *Ceram. Int.* **2021**, *47*, 34501–34507. [CrossRef]
92. Minkov, D.; Vateva, E.; Skordeva, E.; Arsova, D.; Nikiforova, M. Optical properties of Ge-As-S thin films. *J. Non-Cryst. Solids* **1987**, *90*, 481–484. [CrossRef]
93. Ding, G.; Clavero, C.; Schweigert, D.; Le, M. Thickness and microstructure effects in the optical and electrical properties of silver thin films. *AIP Adv.* **2015**, *5*, 117234. [CrossRef]
94. Sıdır, İ.; Sıdır, Y.G.; Berber, H.; Demiray, F. Electronic structure and optical properties of Schiff base hydrazone derivatives by solution technique for optoelectronic devices: Synthesis, experiment and quantum chemical investigation. *J. Mol. Struct.* **2019**, *1176*, 31–46. [CrossRef]
95. Aly, K.A. Optical band gap and refractive index dispersion parameters of $As_xSe_{70}Te_{30-x}$ ($0 \leq x \leq 30$ at.%) amorphous films. *Appl. Phys. A* **2010**, *99*, 913–919. [CrossRef]
96. Shen, Q.; Katayama, K.; Sawada, T.; Toyoda, T. Characterization of electron transfer from CdSe quantum dots to nanostructured TiO2 electrode using a near-field heterodyne transient grating technique. *Thin Solid Films* **2008**, *516*, 5927–5930. [CrossRef]
97. Hassanien, A.S. Studies on dielectric properties, opto-electrical parameters and electronic polarizability of thermally evaporated amorphous $Cd_{50}S_{50-x}Se_x$ thin films. *J. Alloys Compd.* **2016**, *671*, 566–578. [CrossRef]
98. Hamam, K.A.; Mohery, M.; Aly, K.A. New quaternary $Ge_3S_6Ag_{1-x}Sn_x$ ($0.0 \leq x \leq 1$) chalcogenide glasses for optical devices. *Ceram. Int.* **2025**, *51*, 2880–2890. [CrossRef]
99. Alsaif, N.A.M.; Aly, K.A.; Ibraheem, A.A. Linear and non-linear optical properties of (Ge1S2)100-X(As2Te3)X ($0 \leq x \leq 100$) films. *Opt. Mater.* **2024**, *149*, 114972. [CrossRef]
100. Ahmed, M.; Bakry, A.; Qasem, A.; Dalir, H. The main role of thermal annealing in controlling the structural and optical properties of ITO thin film layer. *Opt. Mater.* **2021**, *113*, 110866. [CrossRef]
101. Liu, J.N.; Wu, B.W.; Zhang, B.; Liu, Y. Synthesis and characterization of metal complexes of Cu(II), Ni(II), Zn(II), Co(II), Mn(II) and Cd(II) with tetradentate schiff bases. *Turk. J. Chem.* **2006**, *30*, 41–48.
102. Vogel, A.I. *Vogle's Text Book of Quantitative Chemical Analysis*, 5th ed.; John Wiely & Sons New York, NY, USA, 1989; p. 906.
103. Svehla, G. *Vogel's Textbook of Macro and Semi Micro Quantitative Inorganic Analysis*, 5th ed.; Longman Inc.: New York, NY, USA, 1979; p. 617.
104. Lewis, J.; Wilkins, R.G. *Modern Coordination Chemistry: Principles and Methods*; Interscience Publishers: Geneva, Switzerland, 1960; p. 487.

105. Boggess, R.K.; Zatko, D.A. The use of conductivity data for the structure determination of metal complexes. *J. Chem. Educ.* **1975**, *52*, 649–651. [CrossRef]
106. Richardson, J.H. Multiple-beam interference microscopy of metals by S. Tolansky. *J. Appl. Crystallogr.* **1972**, *5*, 442. [CrossRef]